Cretaceous Research 177 (2026) 106207

Contents lists available at ScienceDirect

Cretaceous Research

journal homepage: www.elsevier.com/locate/CretRes

Integrated carbon isotope stratigraphy and biostratigraphy of Cenomanian to Turonian carbonates from Jordan – An updated age model and sequence stratigraphic correlations with Oman

Tojo Chirakal [a,*], Jihede Haj Messaoud [a], Ali Alibrahim [a], Khalil Ibrahim [b], Carine Grélaud [c], Amir Kalifi [a], John H. Powell [d], Frans van Buchem [a]

[a] King Abdullah University of Science and Technology, Thuwal, Saudi Arabia
[b] Department of Earth and Environmental Sciences, Prince El-Hassan Bin Talal Faculty of Natural Resources and Environment, The Hashemite University, Zarqa 13133, Jordan
[c] Bordeaux INP, ENSEGID, Bordeaux, France
[d] British Geological Survey (BGS), Nottingham, United Kingdom

ARTICLE INFO

Article history:
Received 6 February 2025
Received in revised form
26 July 2025
Accepted in revised form 27 July 2025
Available online 7 August 2025

Keywords:
Carbonates
Chemostratigraphy
OAE 2
Arabian plate
Sequence stratigraphy

ABSTRACT

A new integrated age model of the uppermost Albian to Coniacian Ajlun Group in West-Central Jordan is presented based on four complete outcrop sections along a ~124 km N–S transect. Carbon isotope curves from this work are integrated with published carbon isotope data and constrained by new and existing nannofossil and ammonite biostratigraphy. Key identified carbon isotope events include the Mid-Cenomanian Event 1 (MCE 1), the Oceanic Anoxic Event 2 (OAE 2) at the Cenomanian/Turonian boundary and the Pewsey Event in the middle Turonian. The findings of this study corroborate and revise previous chemostratigraphic definitions in the study area, while also demonstrating a coeval origin of different lithostratigraphic units within the Ajlun Group. On the Arabian Plate scale, a detailed (3rd order) sequence stratigraphic correlation is made between Jordan and time-equivalent strata from the well-studied Natih Formation in Oman. These correlations help to evaluate the relative contributions of eustasy and tectonics on different plate tectonic settings, since the northeastern and eastern margins were heavily influenced by tectonic processes associated with the closure of the Neo-Tethys Ocean. In Oman, the creation of increased accommodation space (ca. 40 m) is observed relative to Jordan commencing in the interval between the MCE 1 and OAE 2. This suggests the onset of tectonic precursor events in Oman during the middle to late Cenomanian interval before the main tectonic phase in the Turonian, resulting in the termination of shallow water carbonate deposition. In contrast, Jordan remained in a largely passive margin setting.

© 2025 The Authors. Published by Elsevier Ltd. This is an open access article under the CC BY license (http://creativecommons.org/licenses/by/4.0/).

1. Introduction

The Upper Cretaceous Cenomanian to Turonian stratigraphic interval, particularly around the Cenomanian/Turonian boundary (CTB), is characterized by extreme environmental conditions within a hot greenhouse climatic regime (Huber et al., 2002, 2018). This includes high sea-surface temperatures (Norris et al., 2002; Forster et al., 2007; Friedrich et al., 2012; O'Brien et al., 2017; Robinson et al., 2019; Křížová et al., 2024) and high eustatic (global) sea levels (Sahagian et al., 1996; Miller et al., 2004, 2005; Haq, 2014; Wendler and Wendler, 2016; Ray et al., 2019). Additionally, the widespread occurrence of dysoxic to anoxic oceanic conditions during the CTB interval are a further reflection of such environmental extremes. This Oceanic Anoxic Event (OAE) 2 represents one of the largest OAE's of the Mesozoic and was caused by major perturbations in the global carbon cycle (Turgeon and Creaser, 2008; Jenkyns, 2010; Li et al., 2022; Matsumoto et al., 2022; Jones et al., 2023; Sooraj et al., 2024; Takashimi et al., 2024; Walker-Trivett et al., 2024). As a result of these anoxic conditions, the OAE 2 is characterized by the global occurrence of organic-rich marine sediments (Schlanger and Jenkyns, 1976; Trabucho Alexandre et al., 2010).

On the margins of the Arabian Plate, global as well as regional environmental fluctuations during the Cenomanian to Turonian

* Corresponding author.
E-mail address: tojo.chirakal@kaust.edu.sa (T. Chirakal).

https://doi.org/10.1016/j.cretres.2025.106207
0195-6671/© 2025 The Authors. Published by Elsevier Ltd. This is an open access article under the CC BY license (http://creativecommons.org/licenses/by/4.0/).

significantly affected carbonate depositional environments and in turn the resulting stratigraphic architecture and facies distributions (van Buchem et al., 2011; Wohlwend et al., 2016; Razin et al., 2017; Hennhoefer et al., 2020; Bromhead et al., 2022). Furthermore, regional tectonic forcings associated with the closure of the Neo-Tethys Ocean introduce an additional parameter significantly affecting carbonate sedimentation on the margins of the Arabian Plate during this stratigraphic interval. This is particularly evident at the plate-scale middle Turonian K 150 sequence boundary (SB) (Sharland et al., 2001; Simmons et al., 2025). Tectonic events associated with the K 150 SB severely impacted shallow water carbonate deposition, especially on the eastern and northeastern margins of the Arabian Plate, which saw an evolution from a passive to an active margin during the Cenomanian to Turonian, eventually resulting in the ophiolite obduction on to the Arabian Plate (Sharland et al., 2001; Razin et al., 2017; Barrier et al., 2018; Bromhead et al., 2022; Searle et al., 2022; Simmons et al., 2025). Contrary to this, the northwestern margin remained in a largely passive margin tectonic setting (Barrier et al., 2018) and shallow water carbonate deposition resumed fairly quickly after the K 150 SB (Powell and Moh'd, 2011).

Long-range sequence stratigraphic correlations across the Arabian Plate provide an improved understanding of the relative impact of varying eustatic versus tectonic forcing mechanisms on large-scale stratigraphic architecture. Additionally, such studies can also offer more precise dating of the onset of tectonic events affecting sedimentation patterns. Moreover, such plate-scale correlations can provide further insights into the timing and controlling mechanisms of depositional events, such as the deposition of organic-rich facies during the OAE 2. However, such long-range studies across the Arabian Plate margins are limited in number and require precise age controls for high-resolution sequence stratigraphic correlations (Bromhead et al., 2022).

Carbon isotope stratigraphy ($^{13}C/^{12}C$ ratios, hereafter noted in the delta notation as $\delta^{13}C$) is a powerful correlation tool that spans intrabasinal to global scales (Scholle and Arthur, 1980; Schlanger et al., 1987; Jarvis et al., 2006, 2015; Wendler et al., 2010; Wendler, 2013) and is therefore well suited for establishing correlations across the Arabian Plate. Furthermore, $\delta^{13}C$-based chemostratigraphy can provide higher temporal resolutions (<100 ka) compared to biostratigraphic methods (Paul and Lamolda, 2009; Cramer and Jarvis, 2020), making it an ideal tool for establishing high-resolution timelines. $\delta^{13}C$ profiles obtained from carbonates reflect, assuming no major influences such as meteoric diagenesis (Swart, 2015; Cramer and Jarvis, 2020), changes in the $\delta^{13}C$ of dissolved inorganic carbon (DIC) from the ancient global ocean. This in turn mirrors perturbations of the global carbon cycle through time (Cramer and Jarvis, 2020). For example, the OAE 2 at the CTB is recognized by a globally recorded major positive $\delta^{13}C$ excursion and provides a major chemostratigraphic anchor point (e.g., Jarvis et al., 2006; Voigt et al., 2008; Jenkyns, 2010; Wendler, 2013; Wohlwend et al., 2016; Metzner et al., 2023).

Despite this potential for long-range correlations and high temporal resolutions, noteworthy differences exist in the availability of $\delta^{13}C$ records for the Cenomanian to Turonian stratigraphic interval between both sides of the Arabian Plate. The northeastern and eastern plate margins, provide a significantly higher number of available carbon isotope curves as well as more complete curves in general (i.e., covering more of the Cenomanian to Turonian interval) (Hajikazemi et al., 2012; Vahrenkamp, 2013; Vincent et al., 2015; Wohlwend et al., 2016; Hairapetian et al., 2018; Hennhoefer et al., 2019; Kalanat and Vaziri-Moghaddam, 2019; Lawa et al., 2023). Contrary to this, the northwestern Arabian Plate margin has received significantly less scientific attention, with the available carbon isotope curves often being stratigraphically limited to the upper Cenomanian to lower Turonian, in order to cover the OAE 2 (Wendler et al., 2010, 2014; El-Sabbagh et al., 2011; Grosheny et al., 2017; Farouk et al., 2025). Consequently, this severely limits the long-range correlation potential of the northwestern Arabian Cenomanian to Turonian succession with coeval strata from the other side of the Arabian Plate as well as other global deposits of the same age.

In Jordan, the Cenomanian to Turonian stratigraphic interval is represented by the Ajlun Group, which outcrops along the western boundary of the country, allowing for detailed basin-scale sedimentological studies (Powell and Moh'd, 2011) (Fig. 1A and B). Despite preserving the complete Cenomanian to Turonian succession, the available carbon isotope stratigraphy is mostly limited to the upper Cenomanian to lower Turonian interval and the few existing studies present discrepancies in their chronostratigraphic interpretations and exhibit conflicting biostratigraphic constraints (Wendler et al., 2010, 2014; Farouk et al., 2017).

This study presents the results of a basin-scale sedimentological and geochemical study of the uppermost Albian to Coniacian Ajlun Group, based on four sedimentary sections along a ~124 km proximal-distal transect in western Jordan (Fig. 1A). The present work is divided into two main parts:

(1) A new Jordanian basin-wide carbon isotope record is presented, constrained by new nannofossil zonation (Messaoud et al., 2025) covering the Cenomanian to Turonian interval. The data set of this work is furthermore augmented by geochemical (Wendler et al., 2014) and biostratigraphic (Nagm et al., 2017) data from previous literature.
(2) Using the results of the first part of this work as a new stratigraphic reference point on the northwestern Arabian Plate margin, the Jordanian results are correlated with a high-quality Cenomanian to Turonian dataset from the other side of the Arabian Plate in Oman (van Buchem et al., 2002, 2011; Wohlwend et al., 2016; Bromhead et al., 2022). This allows for the assessment of the relative impact of tectonics, eustacy and regional environmental factors on the stratigraphic architecture (depocenters and facies distribution) at the scale of the Arabian Plate.

2. Geologic setting

The geomorphology of western Jordan is characterized by the NNE-SSW orientated Dead Sea Transform (DST, Fig. 1A) fault system comprising various subsidiary faults (Al Hseinat et al., 2023). This sinistral, strike-slip fault system represents the northwestern plate boundary of the Arabian Plate with the Sinai microplate (Fig. 1A) and is linked to the opening of the Red Sea during the Miocene (Segev et al., 2014 and references therein; Viltres et al., 2022). Along the eastern DST flank, the Cretaceous to Eocene succession is well exposed from the northern part of the country to the Ras en Naqb escarpment in southern Jordan (Powell and Moh'd, 2011) (Fig. 1A). Given the approximately 105 km sinistral offset, any correlations towards the west, crossing the modern-day DST, must be corrected accordingly (Quennell, 1959; Powell and Moh'd, 2011).

On the eastern side of the DST, the outcropping Cretaceous succession of Jordan comprises the Lower Cretaceous Kurnub and Upper Cretaceous Ajlun and Belqa groups (Fig. 1B), with the latter one also encompassing Paleocene and Eocene strata (Powell and Moh'd, 2011).

During the deposition of the Ajlun Group (upper Albian to Coniacian (Powell and Moh'd, 2011; Messaoud et al., 2025)), present-day Jordan was situated along the southern passive continental margin of the Neo Tethys Ocean in near-equatorial

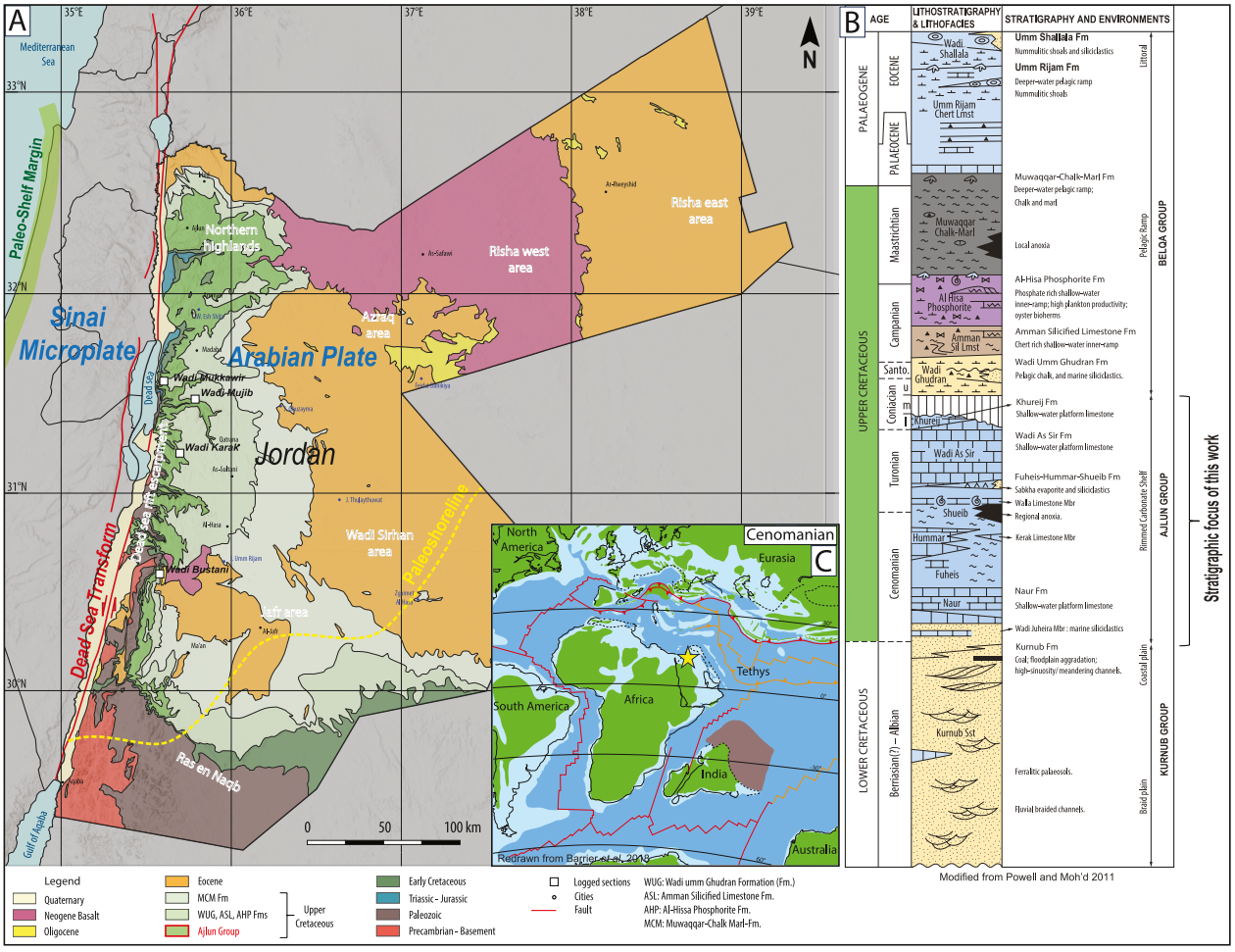

Fig. 1. A: Overview of the study area and logged sections in western Jordan along the Dead Sea Transform (DST). Note the outcropping Ajlun Group along the eastern margin of the DST. The yellow dashed line represents the approximate paleo-shoreline position during the Ajlun deposition, while the thick green line shows the approximate paleo-shelf margin (Flexer et al., 1986; Powell and Moh'd, 2011). B: Simplified lithostratigraphic column of the Cretaceous and Paleogene stratigraphy of western Jordan after Powell and Moh'd (2011). Note the stratigraphic extent of the Ajlun Group marked on the right. C: Paleogeographic reconstruction for the Cenomanian, redrawn and edited from Barrier et al. (2018). The yellow star marks the position of the study area on the Arabian Plate margin. Note the flooded shelf areas (light blue color) around the Arabian Plate.

latitudes (Scotese, 2014; Barrier et al., 2018) (Fig. 1C). Following a largely continental depositional environment in the Lower Cretaceous, forming the Kurnub Group, a major transgression occurred during the late Albian, resulting in large parts of the continental margins of the northwestern Arabian Plate being flooded and initiating the deposition of the Ajlun Group (Powell and Moh'd, 2011). This event occurred with a gradual onlap and marked the establishment of a broad carbonate platform in the Levant region including modern-day Jordan, also termed as the Levant Platform (Kuss, 1992a; 1992b; Buchbinder et al., 2000; Kuss et al., 2003; Schulze et al., 2003; Frank et al., 2010; Powell and Moh'd, 2011). In Jordan, the paleo-shoreline was located in the southern and southeastern part of the country, while the paleo-shelf margin corresponds roughly to the modern-day Mediterranean coastline (Fig. 1A) (Bein and Weiler, 1976; Sass and Bein, 1982; Powell and Moh'd, 2011). Intrashelf basins and topographic highs are reported to have occurred on the Levant Platform during the late Cenomanian to early Turonian in Jordan, the Negev and Sinai (Buchbinder et al., 2000; Bauer et al., 2003; Kuss et al., 2003; Schulze et al., 2005).

Given the overall tectonic setting on a passive continental margin, the study area did not experience the large-scale tectonic deformation during the Cenomanian to Turonian which, in contrast, occurred along the eastern and northeastern Arabian Plate margin (Barrier et al., 2018).

However, initial local compressional tectonics related to the Syrian Arc Fold Belt, an S-shaped fold belt extending from modern-day Syria along the Levant into the Sinai, are generally proposed to have developed during the Turonian (Al Hseinat et al., 2023) and more precisely the late Turonian (Hardy et al., 2010 and references therein), before the main compressional phases occurred later in the Cretaceous and Cenozoic (Frizon De Lamotte et al., 2011).

Even older dates for the initiation of vertical movements related to the Syrian Arc deformation on the Levant Platform are suggested, placing the onset during the late Cenomanian in the Sinai (Bauer et al., 2003) and Israel (Buchbinder et al., 2000), resulting in significant stratigraphic gaps within the CTB interval in those locations. However, in the study area of this work, no comparable tectonic movements affecting sedimentation patterns were observed for the Cenomanian to Turonian interval (Schulze et

al., 2003; Powell and Moh'd, 2011). This is furthermore supported by the stratigraphic data presented later in this work.

3. Stratigraphic framework

The lithostratigraphy of the upper Albian to Coniacian Ajlun Group (Fig. 1B) has been studied since the 20th century based on outcrop data (Quennell, 1951; Wetzel and Morton, 1959; Wolfart, 1959·Masri, 1963; Bender, 1974; Powell, 1989; Kuss, 1992a; Berndt, 2002; Kuss et al., 2003; Schulze et al., 2003; Baaske, 2005; Powell and Moh'd, 2011; Nagm et al., 2017) and subsurface investigations (Andrews, 1992; Abu Saad and Andrews, 1993; Kalifi et al., 2025).

Age dating of the Ajlun Group is largely based on ammonite, calcareous nannofossil and ostracod biostratigraphy (Aly et al., 2008; Morsi and Wendler, 2010; Powell and Moh'd, 2011; Farouk et al., 2017; Nagm et al., 2017 and references therein; Schulze et al., 2003, 2004, Wiese and Schulze, 2005) and to a lesser extent on $\delta^{13}C$ chemostratigraphy in and around the CTB interval (Morsi and Wendler, 2010; Wendler et al., 2010, 2014; Farouk et al., 2017, 2025). The latest, updated biostratigraphic age model for the Ajlun Group, based on new calcareous nannofossils and previous literature is provided by Messaoud et al. (2025). Sequence stratigraphic studies on a basin scale for the Ajlun Group are presented by Schulze et al. (2003) and Powell and Moh'd (2011).

Thicknesses for the Ajlun Group range from <100 m in the southwest of Jordan (Ras en Naqb area) to >450 m in west central Jordan, while subsurface data shows thicknesses in excess of 800 m in the northwest of the country (Andrews, 1992).

The following paragraphs provide an overview on the lithostratigraphy of the Ajlun Group, while Fig. 2–6 provide outcrop photos to illustrate the relevant lithostratigraphic units. An extensive summary on the lithostratigraphy is provided by Powell (1989) and Powell and Moh'd (2011) and the reader is referred to these works for more information.

According to Masri (1963), the lithostratigraphy of the Ajlun Group in western Jordan comprises six formations from base to top (Fig. 1B): the Naur, Fuheis, Hummar, Shueib and Wadi as Sir formations. The Khureij Formation, initially reported locally by Powell (1989) and Powell and Moh'd (2011), has now been identified across the study area of this work (Messaoud et al., 2025).

The base of the Ajlun Group, the uppermost Albian to lower/middle Cenomanian Naur Formation, is subdivided into four members (a, b, c and d) (Powell and Moh'd, 2011). Member a (also named Wadi Juheira), forms a marl and marly limestone dominated unit with increasing amounts of siliciclastics towards the south. Members b and d, and to a lesser extent Member c, form prominent carbonate cliffs in much of the studied landscapes with intercalated marl units (Fig. 3). These carbonate cliffs feature, amongst others, m-scale massive-nodular, bioturbated (*Thalassinoides* burrows, Appendix E 7) beds with wackestone textures. Furthermore, the carbonate cliffs of the Naur Formation also show dm-scale, more recessive beds with wackestone, packstone and locally grainstone textures. Dolomitization occurs in several studied sections within this formation (Powell and Moh'd, 2011).

The marl-dominated middle Cenomanian Fuheis Formation tends to showcase a recessive, slope forming outcrop expression (Figures 2, 5 and 6). A prominent ammonite-bearing carbonate

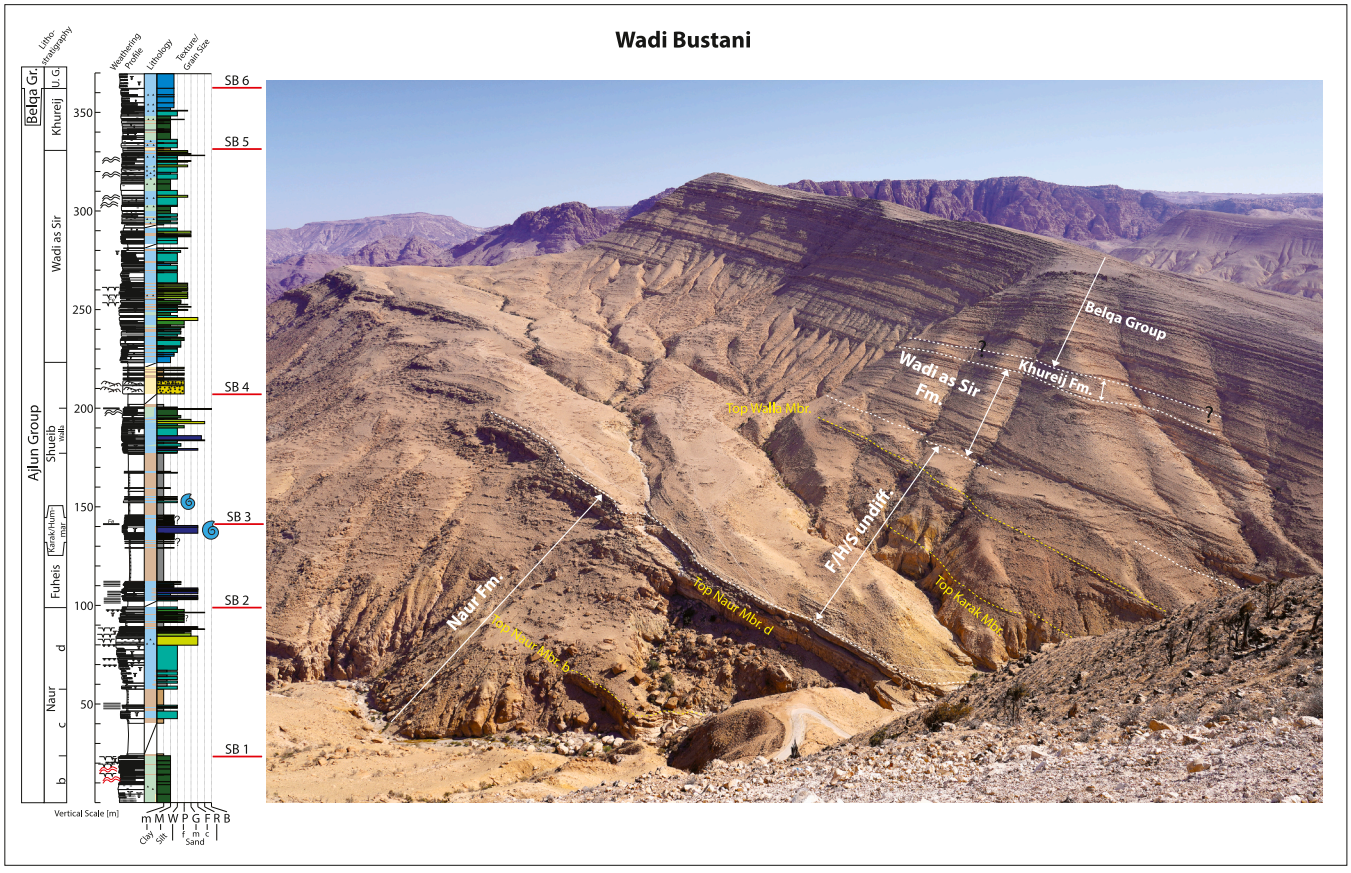

Fig. 2. W. Bustani section looking northeast, featuring the entire Ajlun Group. Note the shallow, slope-forming nature of the Fuheis, Hummar and Shueib (F/H/S) interval. Abbreviations of lithostratigraphic units: U.G: Umm Ghudran Formation. The legend for the outcrop log is shown in Fig. 7. Also note the sequence boundaries in the outcrop log.

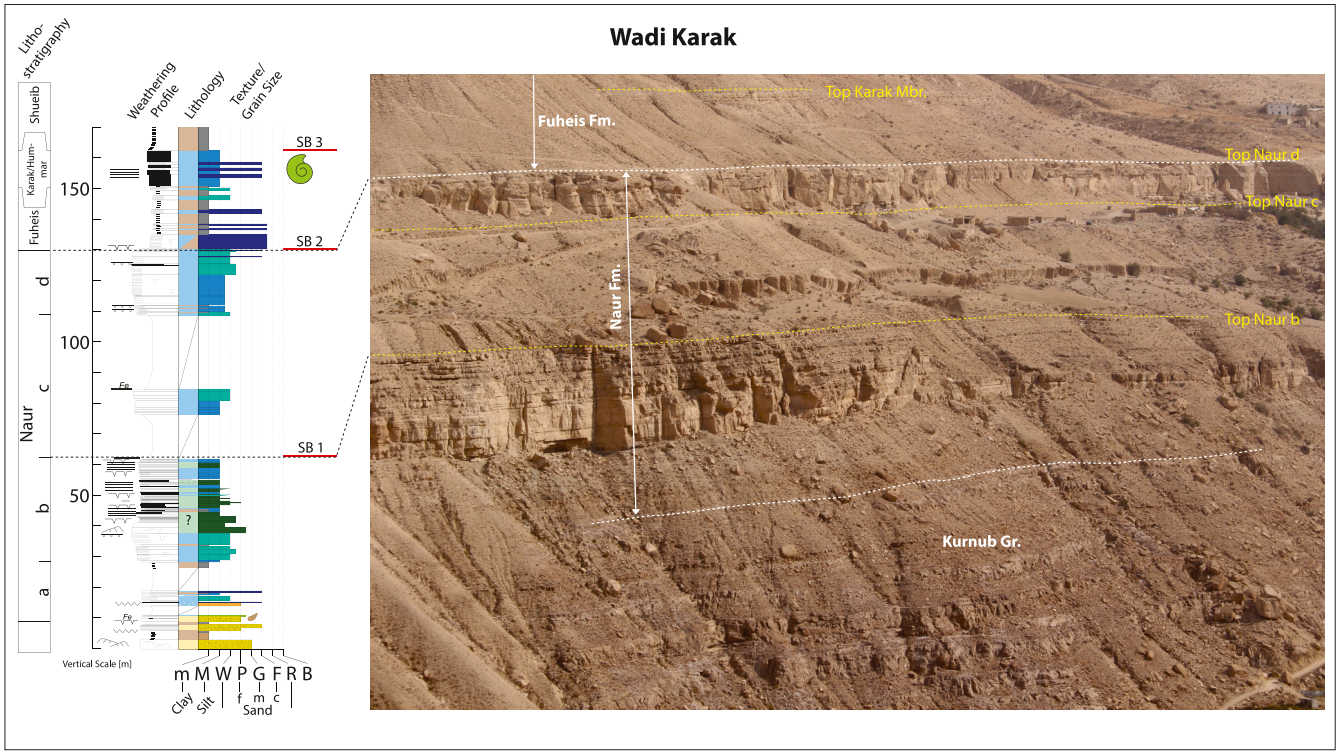

Fig. 3. W. Karak section looking east, Naur Formation. Note the typical three-cliff appearance of members b, d and to a lesser extent Member c. The legend for the outcrop log is shown in Fig. 7. Also note the sequence boundaries in the outcrop log.

unit, the Karak Limestone Member within this formation, represents a regionally mappable feature south of Wadi (W.) Mujib (Fig. 2 and 3) (Powell and Moh'd, 2011).

The overlaying middle Cenomanian Hummar Formation forms a prominent mappable carbonate marker cliff north of W. Mujib and also contains ammonites (Fig. 5 and 6), while carbonate textures comprise mudstones, wackestones and packstones (Powell and Moh'd, 2011).

The upper Cenomanian to middle Turonian Shueib Formation is largely composed of marls and shales and, similar to the Fuheis Formation, shows another recessive, slope-forming outcrop expression. Black/dark marls and shales rich in organic material, associated with the OAE 2 at the CTB, have been reported in several locations within this unit (Schulze et al., 2003; Morsi and Wendler, 2010; Powell and Moh'd, 2011; Wendler et al., 2014). An ammonite-rich lower Turonian limestone unit, the Walla Member, can be traced regionally, including in the studied transect (Fig. 4, termed as Upper Walla Member). The uppermost part of the Shueib Formation features middle Turonian lowstand deposits with fluvial sandstones in southern Jordan, which grade into evaporites found in the central and northern part of the study area (Schulze et al., 2003; Powell and Moh'd, 2011; Messaoud et al., 2025). The top of this formation is well defined by the sharp contact with the overlying carbonate beds of the Wadi as Sir Formation (Fig. 4, 5 and 6).

In literature, the Fuheis, Hummar and Shueib formations are frequently characterized as undifferentiated (also termed F/H/S) south of W. Mujib (Powell, 1989), as the prominent carbonate cliff characterizing the Hummar Formation (consequently dividing the underlying Fuheis and the overlying Shueib formations) thins out rapidly south of W. Mujib. An alternative scheme, amalgamating the Karak Member and the Hummar Formation for the southern study area of this work, has also been proposed (Schulze et al., 2003; Messaoud et al., 2025).

The middle to upper Turonian (Messaoud et al., 2025) Wadi as Sir Formation is dominantly composed of stacked dm-scale carbonate beds and crops out prominently along the entire study area (Fig. 2, 4, 5 and 6). Carbonate rock textures comprise mudstones, wackestones, packstones and locally oolithic grainstones (Powell and Moh'd, 2011).

The Coniacian aged Khureij Formation was initially reported locally by Powell (1989) and Powell and Moh'd (2011), and has recently been identified along the studied transect of this work (Messaoud et al., 2025). The formation shows more recessive but otherwise similar bedding patterns (Fig. 6) and textures as the above-described Wadi as Sir Formation (Powell, 1989; Powell and Moh'd, 2011).

The Ajlun sequence is terminated by a prominent drowning unconformity, where Coniacian pelagic chalks of the Belqa Group overlie the shallow water carbonates of the Ajlun Group (Fig 1B) (Powell, 1989; Powell and Moh'd, 2011).

4. Methods

4.1. Locations and sedimentological logging

Field work was carried out on four sections in west-central Jordan along the eastern DST margin (Fig. 1A): W. Bustani, W. Karak, W. Mujib and W. Mukkawir.

W. Bustani and W. Mujib were logged as continuous section, while W. Karak and W. Mukkawir represent composite sections (see Appendix B and D and Table 1). An overview on the logged thickness and number of analyzed data is shown in Table 2.

Sedimentological logging during field work was performed on a dm-scale (1:100), and if necessary, a cm-scale resolution. Particular emphasis was placed on bedding and weathering pattern, lithology, grain size, carbonate rock texture (Dunham, 1962; Embry and Klovan, 1971), bioturbation, color and secondary minerals (e.

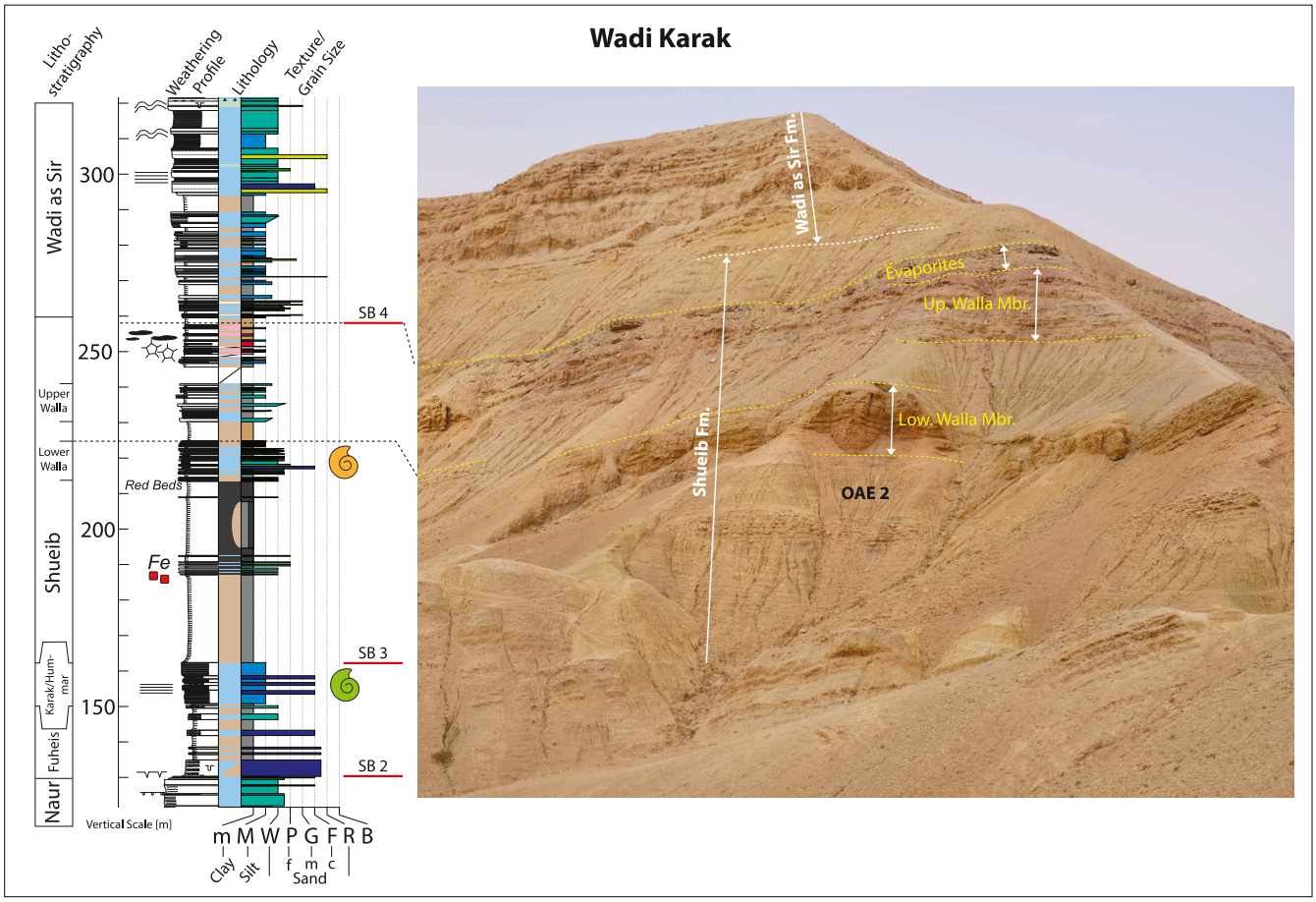

Fig. 4. W. Karak section, looking north: Fuheis/Hummar/Shueib interval studied by Wendler et al. (2014). Note the thick evaporite unit on top of the Upper Walla Member. The legend for the outcrop log is shown in Fig. 7. Also note the sequence boundaries in the outcrop log.

g., glauconite or gypsum). Additionally, sedimentary and stratigraphic surfaces (iron crusts, erosive surfaces, hardgrounds, bioturbated surfaces and exposure surfaces) were also recorded (Strasser et al., 1999), while carbonate components were differentiated between non-skeletal (e.g., ooids or peloids) and skeletal components (e.g., benthic fauna, benthic foraminifera, "builders" such as in-situ corals and pelagic fauna). Carbonate components were semi-quantified by differentiating between "rare", "common" and "abundant". For microfacies observations, 321 thin sections were prepared from collected rock samples. Each thin section was impregnated with blue epoxy to visualize porosity and partially stained with Alizarin Red S, in order to visually differentiate between aragonite/calcite and dolomite. The descriptive attributes for microfacies analysis were based on the same sedimentary attributes described above for the field work.

4.2. Carbon isotope analysis

$\delta^{13}C$ and $\delta^{18}O$ analysis was carried out on bulk rock samples collected during field work with variable sampling density, generally ranging between dm and m-scale. Table 2 shows the number of analyzed rock samples per section. Whole rock powder samples were obtained using a handheld electric drill with a diamond cutting wheel. The measurements were conducted at the University of Miami (FL, USA) in the laboratory of Professor Peter K. Swart. The analytical procedure comprised treating the sampled bulk rock powder samples with phosphoric acid in a standard acid bath at 90 °C. The CO_2 gas was subsequently analyzed with a dual-inlet *Finnigan-MAT 251* mass spectrometer (Thermo Fisher Scientific, Waltham, MA, USA) (Swart et al., 1991). Calibration of the CO_2 gas produced from the carbonates was achieved with NBS-19 (National Bureau of Standards) and corrected for isobaric interferences (Brand et al., 2010). Repeated measurements provided a precision of <0.1 ‰ for carbon and oxygen isotope values. Resulting values are reported using the standard delta (δ) notation [‰] relative to the Vienna-Pee-Dee-Belemnite (VPDB).

4.3. RockEval pyrolysis

Pyrolysis was performed on bulk rock samples to study total organic carbon (TOC) concentrations in selected intervals covering the CTB. Table 2 shows the number of measured samples for each studied section. Each powder sample was obtained using a handheld electric drill with a diamond cutting wheel. Pyrolysis was performed using a *RockEval 7S* analyzer (Vinci Technologies, Nanterre, France) at the King Abdullah University of Science & Technology (Saudi Arabia) following the procedure outlined in Behar et al. (2001). The obtained results are given in wt.-%.

5. Results

In order to establish an integrated age model of the Ajlun Group, four fully exposed and complete outcrop sections have

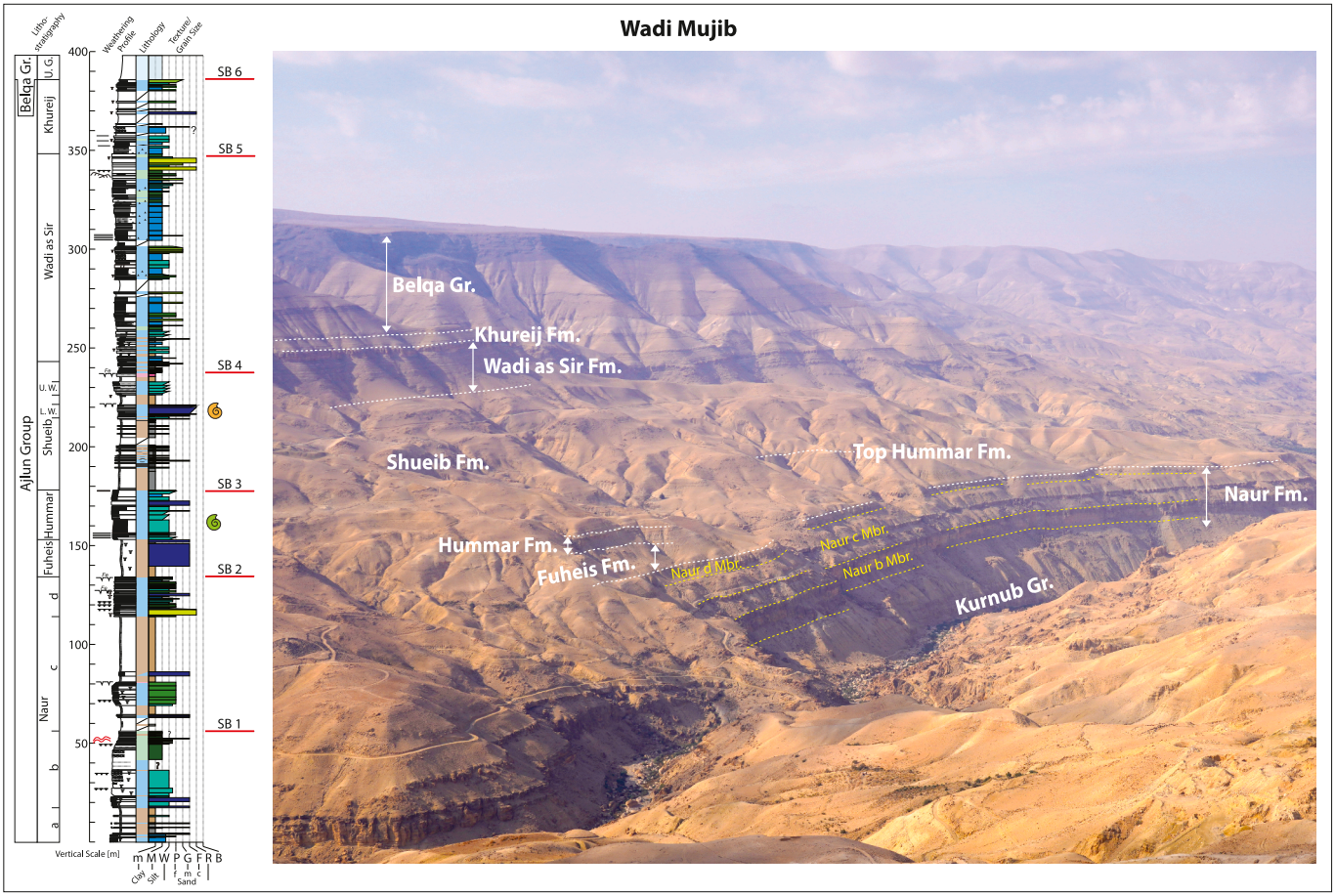

Fig. 5. W. Mujib section looking southwest, showing the entire Ajlun Group succession. Note the cliff forming Naur, Hummar and Wadi as Sir formations, while the marl and shale-dominated Fuheis and Shueib formations tend to form more recessive and gentle slopes in the landscape. Much of the ground between the top of the Hummar Formation and the base of the Wadi as Sir Formation is obscured by shallow landslips. Abbreviations of lithostratigraphic units: L. W.: Lower Walla Member, U. W.: Upper Walla Member and U. G.: Umm Ghudran Formation. The legend for the outcrop log is shown in Fig. 7. Also note the sequence boundaries in the outcrop log.

been studied for their (5.1) lithostratigraphy and regionally expressed sequence boundaries, (5.2) biostratigraphy and (5.3) carbon isotope stratigraphy.

Figure 7 presents a basin-scale correlation along west-central Jordan, integrating the chemo- and biostratigraphic constraints presented in this work within a sequence stratigraphic framework. The individual logs for each section are shown in Appendix A – D.

5.1. Outcrop description and sequence boundaries

The studied sections generally feature excellent outcrop quality (Fig. 2–6), allowing for almost continuous sedimentological logging. The adopted lithostratigraphy of this work, generally reflects the main lithological units described by previous authors summarized in Section 3 (Fig. 1B). Notable exceptions include the Karak Member within the Fuheis Formation and the Hummar Formation. As noted in Section 3, both are often regarded as two distinct lithostratigraphic units in the literature (e.g., Powell and Moh'd, 2011; Farouk et al., 2017). Here, we interpret the Karak Member as the proximal, lateral equivalent to the Hummar Formation (see Section 6.1). This is also supported by data from Schulze et al. (2003) and Messaoud et al. (2025). Additionally, disagreement exists regarding the lithostratigraphic definition of the Naur Formation and Karak Member in W. Karak between this work and Farouk et al. (2017), who interpret the uppermost Naur Member d as the Karak Member (see Fig. 3 in their study and compare to Fig. 3 in this work). Similarly, different lithostratigraphic definitions exist for the W. Mukkawir section, where Schulze et al. (2003) place the uppermost Naur Member within the Hummar Formation of this study (see Fig. 9a in their study and compare to Fig. 6 in this work). This is also in disagreement with previous work by Powell and Moh'd (2011). The stratigraphic terminology of a lower (regional marker bed containing ammonites) and upper Walla Member as used by Wendler et al. (2014) is henceforth applied in this study.

Since the purpose of this study is to propose an age model, the detailed sedimentology will only briefly be mentioned. A total of 17 lithofacies types are identified based on field- and microfacies observations, covering siliciclastics, evaporite, shallow water carbonate, marly/shaly and chalky lithologies (Fig. 7, Legend), which largely follow previously recognized facies types from earlier studies (Powell, 1989; Kuss, 1992b; Schulze et al., 2003, 2005; Powell and Moh'd, 2011; Farouk et al., 2017). For more detailed information on the general sedimentology and depositional environments of the Ajlun Group, the reader is referred to these works.

The clear lithological changes of regional extent, as shown in the studied outcrop sections (Fig. 2–6), suggest major regional sequence boundaries, which mostly follow those described from previous workers (Schulze et al., 2003; Powell and Moh'd, 2011). Six sequence boundaries provide regional-scale sequence stratigraphic time lines for the studied sections, bounding six sequences (Sequences 1–6, Fig. 7). Ages are based on work from Messaoud et al. (2025).

Fig. 6. W. Mukkawir section looking north showing the entire Ajlun Group. Note the cliff-forming nature of the Naur, Hummar and Wadi as Sir formations. Also note the Dead Sea in distance. Abbreviations of lithostratigraphic units: U. G.: Umm Ghudran Formation. The legend for the outcrop log is shown in Fig. 7. Also note the sequence boundaries in the outcrop log.

Table 1
Coordinates of the studied sections.

Location	Composite Section	Stratigraphy Covered	Coordinates
W. Bustani	Continuous	Naur to Khureij	Lat: 30.597749° long: 35.567108°
W. Karak	W. Karak 1	Naur	Lat: 31.228854° long: 35.662555°
	W. Karak 2	Fuheis to Shueib	Lat: 31.257499° long: 35.591327°
	W. Karak 3	Shueib to Khureij	Lat: 31.204301° long: 35.696865°
W. Mujib	Continuous	Naur to Khureij	Lat: 31.446958° long: 35.782568°
W. Mukkawir	W. Mukkawir 1	Naur to Fuheis	Lat: 31.596078° long: 35.578923°
	W. Mukkawir 2	Hummar to Khureij	Lat: 31.567072° long: 35.605733°

Table 2
Overview of data sets used in this study.

Section	Measured Thickness [m]	Thin Sections	Isotope Samples ($\delta^{13}C$ and $\delta^{18}O$)	TOC Measurements
W. Bustani	370	152	119	48
W. Karak	455	–	a	a
W. Mujib	400	169	182	30
W. Mukkawir	530	–	48	46
Total	1755	321	349	124

[a] Isotope and total organic carbon data obtained from Wendler et al., (2014).

SB 1 (lower Cenomanian) is located on top of the Naur b Member, showing a regionally observable vertical facies transition from heavily bioturbated m-scale beds (mostly algal-bioclastic wackestones) into more recessive (dm-thick) bedded facies with common algal mats, wavy laminations and exposure surfaces, in turn topped by a sharp transition into overlying marls, which represents SB 1. Note that the positioning of this SB 1 in W. Mukkawir is challenging and hence tentative, due to insufficient outcrop exposure resulting from debris cover (Fig. 7). The positioning of a regional SB (here SB 1) on top of Naur Member b agrees with a previous sequence stratigraphic work (see CeJo1 in Schulze et al. (2003)).

SB 2 (around the lower/middle Cenomanian boundary) is positioned at the top of the Naur Formation (Member d). Generally, the vertical evolution within Member d shows a similar bedding pattern as described above, featuring a transition from m-scale massive-bioturbated mudstone and wackestone beds to more recessive dm-scale bedding towards the top. In W. Bustani, the upper part of this member is notably thicker than in W. Mujib and features grainier (packstones, grainstones) facies with abundant benthic foraminifera as well as rudist floatstones (Fig. 7). In

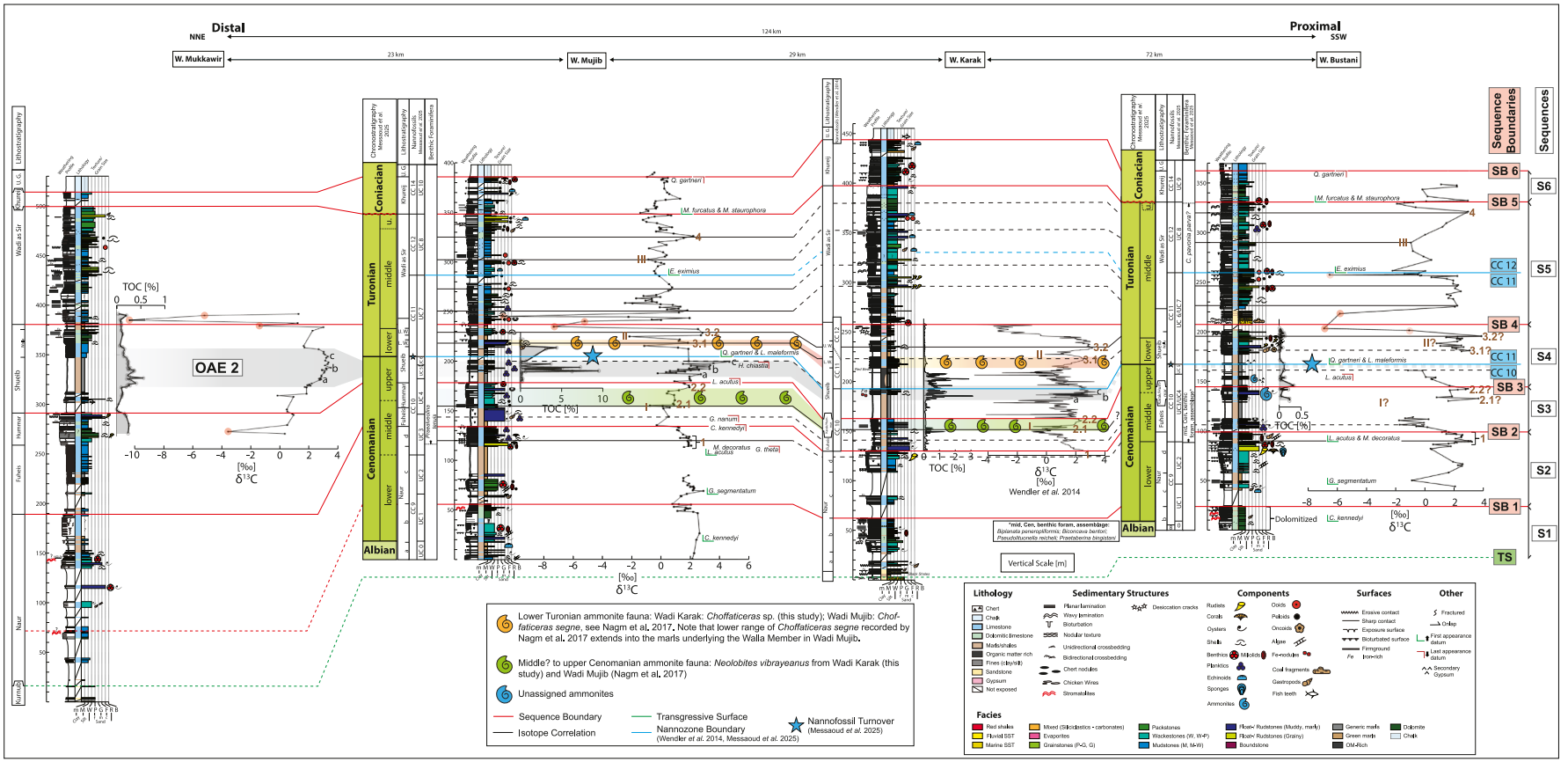

Fig. 7. Intrabasinal correlation between the Jordanian sections. See Fig. 1A for locations. SB 4 is chosen as the datum for this transect. Chronostratigraphic and biostratigraphic columns are based on the respective authors cited in each column. The CC 10/11 nannofossil boundary in W. Karak is based on Wendler et al. (2014) and on Messaoud et al. (2025) in W. Bustani and W. Mujib, while the CC 11/12 boundary is based on Messaoud et al. (2025). The carbon isotope and TOC curve from W. Karak are reproduced from Wendler et al. (2014). Abbreviations of lithostratigraphic units: L. W.: Lower Walla Member, U. W.: Upper Walla Member and U. G. Umm Ghudran Formation. Abbreviations of nannofossils (Messaoud et al., 2025): *C. kennedyi*: *Corollithion kennedyi*, *G. segmentatum*: *Gartnerago segmentatum*, *L. acutus*: *Lithraphidites acutus*, *M. decoratus*: *Microrhabdulus decoratus*, *G. theta*: *Gartnerago theta*, *G. nanum*: *Gartnerago nanum*, *H. chiastia*: *Helenea chiastia*, *Q. gartneri*: *Quadrum gartneri*, *L. maleformis*: *Lucianorhabdus maleformis*, *E. eximius*: *Eiffellithus eximius*, *M. furcatus*: *Marthasterites furcatus*, *M. staurophora*: *Micula staurophora*. Also note the differing horizontal scales for the TOC concentrations.

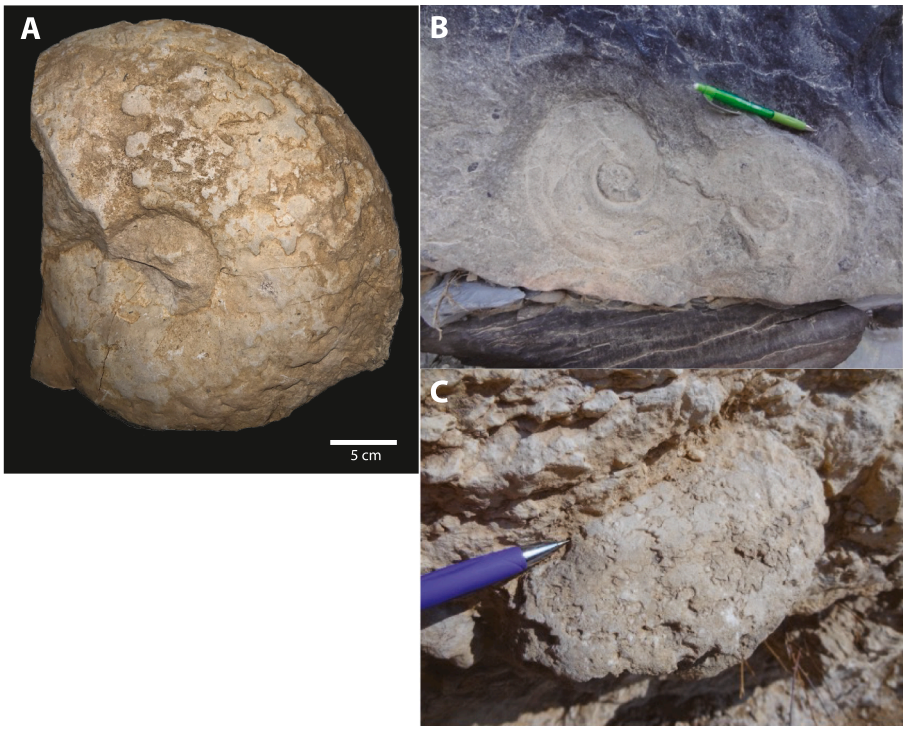

Fig. 8. Ammonite fauna from the W. Karak section, this work. (A–B) *Neolobites vibrayeanus* within the Karak Member (middle? – upper Cenomanian). (C) *Choffaticeras* sp. from the lower Walla Member (lower Turonian).

W. Mujib, the lower interval composed of bioturbated and more massive bedding is significantly thinner compared to the more proximal sections. Moreover, this lower interval is characterized with bioclastic rudstones composed of coral fragments and benthic foraminifera and not bioclastic-algal wackestones as in W. Karak or W. Bustani. The upper part of this member consisting of a more recessive dm-scale bedded interval, features wackestones and packstones rich in planktic foraminifera. The top of the Naur Formation (Mbr d.) is again characterized by a sharp transition into marly facies along the studied transect, locally accompanied by iron-rich surfaces, marking SB 2 (Fig. 7). The placement of a regional SB (SB 2 of this work) at the top of the Naur Member d is also proposed by previous workers (see CeJo2 in Schulze et al. (2003) and SB 2 in Powell and Moh'd (2011)).

SB 3 (upper Cenomanian) is situated on top of the Hummar Formation in W. Mujib and W. Mukkawir and on top of the Karak Member in W. Bustani and W. Karak. It features a sharp transition from shallow water carbonates (mostly mudstones or wackestones) into overlying marls in W. Karak, W. Mujib and W. Mukkawir and to lesser degree in W. Bustani, where thin cm-thick mud-to wackestone beds occur above SB 3 (Fig. 7). The assumption of a coeval origin is supported by biostratigraphy (Nagm et al., 2017; Messaoud et al., 2025), our new chemostratigraphic correlations (see Section 6.1) and data from Schulze et al. (2003), with the previous authors also placing a regional SB (here SB 3) on the top of the Hummar Formation (see their CeJo4). However, note that discrepancies exist between the lithostratigraphic definitions of Schulze et al. (2003) and this work (see earlier this section).

SB 4 (middle Turonian) is placed in the uppermost Shueib Formation and reflects a regionally observable lowstand in the form of siliciclastic and evaporitic lithologies extending into the countries surrounding Jordan (Buchbinder et al., 2000; Bauer et al., 2003; Kuss et al., 2003; Schulze et al., 2003; Powell and Moh'd, 2011). This major SB is also recognized by previous sequence stratigraphic works in Jordan (see TuJo 2 in Schulze et al. (2003) and SB 3 in Powell and Moh'd (2011)) and is equivalent to the K150 SB on the Arabian Plate scale (Sharland et al., 2001; Bromhead et al., 2022; Simmons et al., 2025).

SB 5 (around the Turonian/Coniacian boundary) coincides with the top of the Wadi as Sir Formation and shows a subtle shift from dm-stacked carbonates into more recessive lithologies of the Khureij Formation with otherwise similar bedding patterns (Fig. 7). In W. Bustani and W. Mujib, SB 5 is associated with a significant ca. 400 kyr-long hiatus at this position, as evident from the absence of the CC 13 nannozone (Messaoud et al., 2025). This SB is equivalent to the SB 4 proposed by Powell and Moh'd (2011), which is placed on top of the Wadi as Sir and locally the Khureij Formation (Note that the above-mentioned authors recorded the Khureij Formation only locally, whereas this study identifies it along the entire studied transect, Fig. 7).

SB 6 (Coniacian) reflects the transition from the Ajlun Group shallow water carbonates (Khureij Formation) to the overlying predominantly pelagic Belqa Group (Fig. 7). In the central and northern transect (W. Karak to W. Mukkawir), a sudden shift into pelagic chalk is evident, marking a major regional SB. The lateral continuation of this surface in the more proximal W. Bustani section is more subtle and located at the base of a thick massive bioturbated mudstone unit (Fig. 7) (Messaoud et al., 2025). As mentioned above, this SB is equivalent to SB 4 by Powell and Moh'd (2011).

5.2. Biostratigraphy

A robust multi-proxy biostratigraphic framework is an integral part of the age model presented in this work by constraining and supporting chemostratigraphic interpretations. The recently

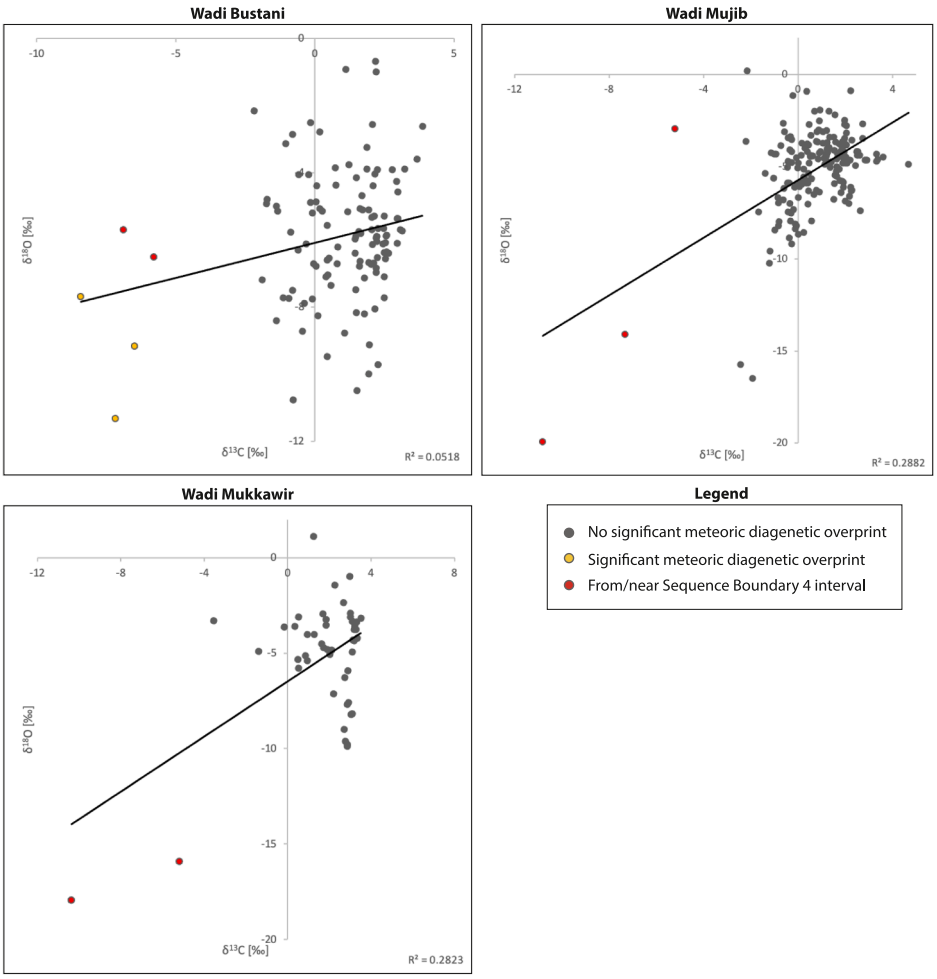

Fig. 9. Carbon and oxygen isotope Crossplots. Red dots mark extreme negative carbon isotope outliers associated with SB 4 (Fig. 7) and orange dots highlight clearly diagenetically influenced values. R^2 values without these red and orange dots (outliers) are shown in text.

published biostratigraphic scheme by Messaoud et al. (2025), based primarily on calcareous nannofossils and supported by benthic foraminifera from the W. Bustani (spanning nannofossil zones CC 8 – CC 14) and W. Mujib (CC 9 – CC 14) sections, provides the basis for the biostratigraphic framework used within this study (Fig. 7). For the W. Karak section, nannofossil stratigraphy from Wendler et al. (2014) is utilized for the Fuheis, Hummar and Shueib interval (Fig. 7 and Appendix B). For detailed information, the reader is referred to both aforementioned works. Further biostratigraphic constraints relevant to this work are outlined below. A taxonomic list of the fossil groups identified within this work is furthermore shown in Appendix F.

Among these, the occurrence of the benthic foraminifer *Praealveolina tenuis*, found in Wadi Mujib at ca. 115 m, is indicative of a middle Cenomanian age (Philip et al., 1995; Bromhead et al., 2022).

Ammonite stratigraphy is used to further complement the above-mentioned largely nannofossil-based biostratigraphic scheme, with data from W. Karak (this work) and W. Mujib (Nagm et al., 2017) comprising the two regionally extensive ammonite marker units: (a) the middle?-upper Cenomanian Karak Member/Hummar Formation and (b) the lower Turonian Walla Member (see the green and orange ammonite zones respectively, Fig. 7).

The (a) Karak/Hummar unit contains *Neolobites vibrayeanus* in W. Karak (Fig. 8 A-B) and W. Mujib (Nagm et al., 2017). The first occurrence (FO) of this ammonite species is commonly attributed to the middle/upper Cenomanian boundary and its range corresponds to the *Calycoceras guerangeri* standard ammonite zone in Europe (Wiese and Schulze, 2005; Meister and Piuz, 2015; Nagm et al., 2017). However, a wider stratigraphic range in Jordan extending downwards to the middle Cenomanian (corresponding to the European *Acanthoceras rhotomagense* and the above lying *Acanthoceras jukesbrownei* zones) is presented in Schulze et al. (2003).

The identified ammonite fauna within (b) the lower Turonian Walla Member in W. Karak comprises *Choffaticeras* sp. (Fig. 8C), while *Choffaticeras segne* has been identified below and within the Walla Member in W. Mujib (Nagm et al., 2017). Although no identification to a species level was possible in W. Karak, the range of the genus is typically constrained to the lower Turonian (Schulze et al., 2003, 2004; Nagm et al., 2017). *Choffaticeras segne* corresponds to the European *Watinoceras devonense* and *Mammites nodosoides* zones (Nagm et al., 2017).

Other ammonites are documented within the Karak Member in W. Bustani (Fig. 7). However, identification of those ammonites was not possible.

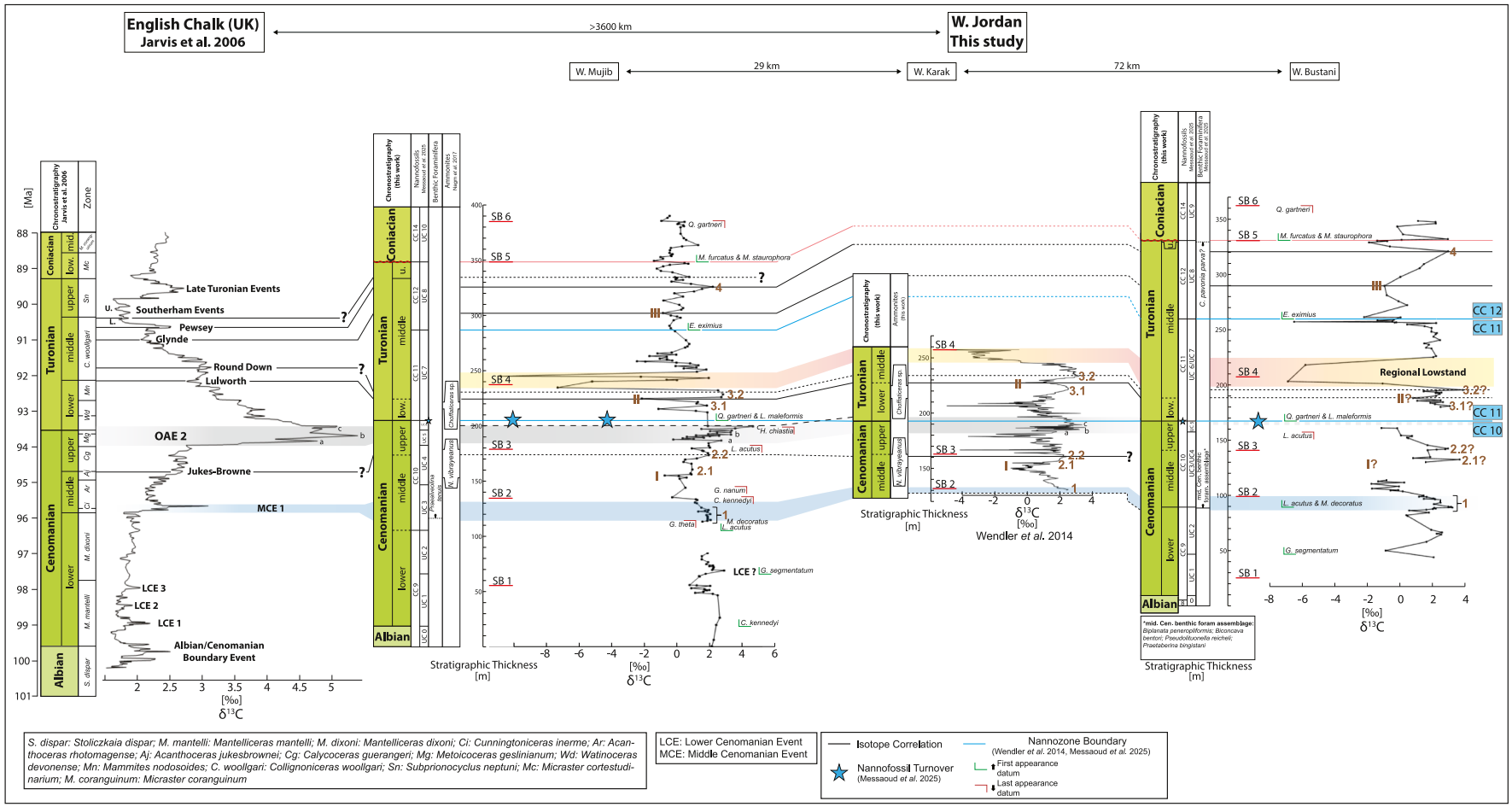

Fig. 10. Global, interbasinal, correlation between Jordan and the UK (English Chalk). Note that the Jordanian sections represent stratigraphic thickness, while the English Chalk curve is shown in time. Chronostratigraphic placements in Jordan are based on the interpretations from this work, founded upon the data from this study and previous workers (see text for more information). The CC 10/11 nannofossil boundary in W. Karak is based on Wendler et al. (2014) and on Messaoud et al. (2025) in W. Bustani and W. Mujib, while the CC 11/12 boundary is based on Messaoud et al. (2025). The carbon isotope curve for the English Chalk reference curve is reproduced from Jarvis et al. (2006), while the carbon isotope curve from W. Karak is reproduced from Wendler et al. (2014). Abbreviations of nannofossils (Messaoud et al., 2025): *C. kennedyi*: *Corollithion kennedyi*, *G. segmentatum*: *Gartnerago segmentatum*, *L. acutus*: *Lithraphidites acutus*, *M. decoratus*: *Microrhabdulus decoratus*, *G. theta*: *Gartnerago theta*, *G. nanum*: *Gartnerago nanum*, *H. chiastia*: *Helenea chiastia*, *Q. gartneri*: *Quadrum gartneri*, *L. maleformis*: *Lucianorhabdus maleformis*, *E. eximius*: *Eiffellithus eximius*, *M. furcatus*: *Marthasterites furcatus*, *M. staurophora*: *Micula staurophora*.

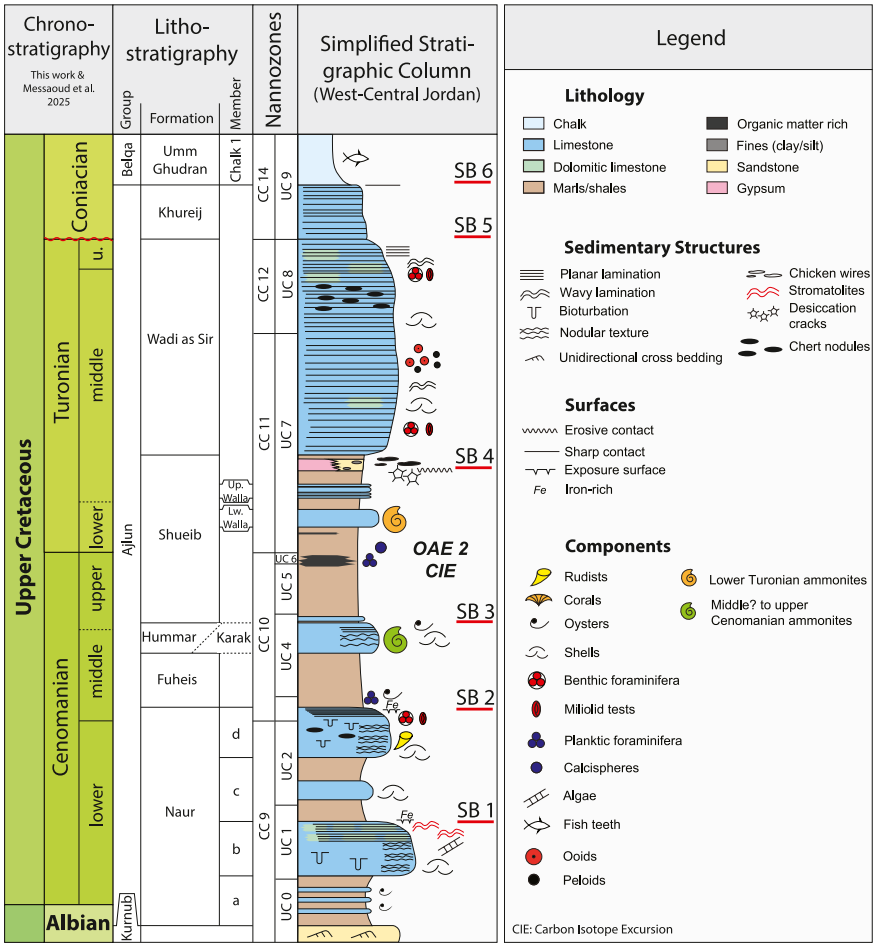

Fig. 11. Updated and simplified lithostratigraphic column of the Ajlun Group, based on the interpretations from this work, see text for details.

5.3. Carbon isotope data

5.3.1. Diagenetic alteration and validity of carbon isotope data

Carbon isotopes of shallow water carbonates are generally less prone to diagenetic alteration than oxygen isotopes (Swart, 2015). Nonetheless, any potential diagenetic factors altering the original $\delta^{13}C$ signal, reflecting the global ocean's DIC during deposition, must be evaluated (e.g., Wendler, 2013). Additional local and/or regional factors which can result in $\delta^{13}C$ values differing from the global signal include, amongst others, mineralogical variations of the carbonate matrix (e.g., higher aragonite fractions resulting in higher $\delta^{13}C$ values (Swart, 2015)) or skeletal compositions between different organisms (Wendler, 2013 and references therein). Moreover, locally/regionally differing $\delta^{13}C$ sea water compositions can also influence measured bulk rock carbon isotope values (Immenhauser et al., 2003; Swart, 2015).

All studied $\delta^{13}C$ curves excluding obvious outliers are presented in Fig. 7. For individual carbon isotope curves with all outliers, see Appendix A – D. The new carbon isotope curves from W. Bustani, W. Mujib and W. Mukkawir as well as W. Karak extracted from Wendler et al. (2014), show similar $\delta^{13}C$ values and long-term trends between each other (Fig. 7). This overall similarity indicates similar depositional and post-depositional (i.e., diagenetic) processes affecting the $\delta^{13}C$ values throughout the studied transect.

Of particular interest are the sudden and pronounced extreme negative $\delta^{13}C$ shifts observable in all studied sections in several intervals (Fig. 7, Appendix A – D). Decreasing $\delta^{13}C$ values are often associated with soil-derived pore waters enriched in ^{12}C (Allan and Matthews, 1982; Immenhauser et al., 2008; Cramer and Jarvis, 2020). Consequently, such drastic negative shifts can be expected to be observed in increased frequency near sequence boundaries, indicating meteoric diagenesis in response to sea level changes (Jarvis et al., 2015). The most significant sudden negative $\delta^{13}C$ shifts occur near or at SB 4, the regionally extensive lowstand observable throughout the studied transect, characterized by marine siliciclastics and supratidal deposits (Fig. 7). Given the non-carbonate lithologies and the evident subaerial influence (e.g., desiccation cracks in W. Karak, Appendix E 2), the $\delta^{13}C$ values near/at SB 4 cannot be correlated globally, but do show a correlation potential of regional significance due to the synchronous stratigraphic appearance (see Section 6.1).

$\delta^{13}C$ versus $\delta^{18}O$ crossplots are commonly used to assess any potential diagenetic overprint (Vahrenkamp, 2010; Huck et al., 2013; Hennhoefer et al., 2019; Kalanat and Vaziri-Moghaddam, 2019; Metzner et al., 2023). Crossplots for the studied sections (Fig. 9) show no relevant correlations between $\delta^{13}C$ and $\delta^{18}O$ values for W. Bustani featuring $R^2 = 0.0518$, W. Mujib $R^2 = 0.2882$ and W. Mukkawir $R^2 = 0.2823$. While such weak/very weak correlations are often used as an indicator for no/low diagenetic overprint (Huck et al., 2013), it is important to emphasize that this approach can be sensitive to a relatively low number of outliers, which are located outside the zone where the majority of samples are situated. Indeed, by removing the extreme negative values associated with the middle Turonian lowstand at SB 4 (red dots in

Fig. 9) and those associated with other zones affected by meteoric diagenesis (evident from secondary gypsum, strong dissolution, meteoric cements and exposure surfaces, see orange dots in Fig. 9), the R^2 values change as follows: W. Bustani: $R^2 = 0.0055$, W. Mujib: $R^2 = 0.12$ and W. Mukkawir: $R^2 = 0.0353$. Overall, such very weak/weak correlations indicate the studied carbonate lithologies where subject to a low degree of diagenetic overprint. Additionally, a comparison with a global reference curve, constrained independently by biostratigraphic zones and markers (Fig. 10), allows to correlate several prominent carbon isotope events (see Section 6.1), further supporting the validity of the presented $\delta^{13}C$ curves as a chemostratigraphic tool.

5.3.2. Carbon isotope curves and TOC

Stratigraphic coverage of $\delta^{13}C$ curves for the Ajlun Group between the studied sections varies from largely complete (W. Bustani and W. Mujib) to focused on the Fuheis, Hummar and Shueib interval covering the CTB and OAE 2 (W. Karak and W. Mukkawir). Data gaps due to a lack of sufficient outcrop quality or obvious diagenetic alteration (e.g., cross cutting secondary gypsum) occur in W. Bustani (ca. 120 and 170 m respectively) and W. Mujib (ca. 100 m, Fig. 7).

As mentioned earlier, $\delta^{13}C$ and TOC data for the W. Karak section are obtained from Wendler et al. (2014). While no perfect stratigraphic overlap between the logged section of this work and Wendler et al. (2014) exists (up to ca. 10 m, see the correlation between the outcrop logs between this work and the aforementioned authors in Appendix B), the present overlap between both works is regarded as sufficient enough for the purpose of this work. This is because the interval of interest, the OAE 2 interval, is litho- and biostratigraphically well constrained in both studies, mainly by the ammonite-bearing Karak Member (middle? – upper Cenomanian *Neolobites vibrayeanus*) below and Walla Member (lower Turonian *Choffaticeras* sp.) above (see green and orange ammonite zones, Fig. 7). For additional information on the curves shown in W. Karak, the reader is referred to Wendler et al. (2014).

The $\delta^{13}C$ values for all studied sections mostly oscillate between ca. −2 to +3.5 ‰ and long-term trends show generally moderate to high degrees of similarity (Fig. 7). Significant short-term negative $\delta^{13}C$ spikes occur in all studied sections, while more pronounced extreme negative shifts occur at/around SB 4 throughout the studied transect, suggesting a synchronous occurrence (SB 4 in all sections, Fig. 7).

Figure 7 furthermore shows TOC values measured in W. Bustani, W. Mujib and W. Mukkawir, while TOC data for W. Karak is obtained from Wendler et al. (2014). The stratigraphic coverage focuses on the Karak/Hummar and Shueib interval in W. Bustani, Fuheis, Karak/Hummar and Shueib interval in W. Karak, much of the Shueib Formation in W. Mujib and the Hummar and Shueib formations in W. Mukkawir.

TOC results at the CTB generally show low values in W. Bustani and W. Mukkawir with <0.5 wt.-% TOC, moderate concentrations in W. Karak with up to ca. 3 wt.-% and high TOC measurements in W. Mujib reaching 9.5 wt.-%.

Following the CTB interval, moderate to high TOC values occur in both W. Karak (<3 wt.-%) and W. Mujib (<4.5 wt.-%) within the lower Turonian, before falling to very low values within the lower Walla Member interval.

6. Discussion

6.1. Integrated age model of the Ajlun Group (Jordan)

Based on a multi-proxy approach, the age model is discussed by integrating carbon isotope and biostratigraphic constraints within a regional sequence stratigraphic framework (Fig. 7). This integrated approach helps to corroborate different stratigraphic correlations and furthermore prevents “wiggle matching” (Wendler, 2013; Jarvis et al., 2015; Cramer and Jarvis, 2020) when correlating between different regional as well as globally distributed $\delta^{13}C$ curves.

The following discussion on the integrated carbon isotope stratigraphy is segmented by the sequences (1–6) bounded by the above-described sequence boundaries (SB 1–6) as shown in Fig. 7. Figure 10 shows the $\delta^{13}C$ correlations between Jordan and the English Chalk (UK) as well as the resulting chronostratigraphic placements for the studied sections from this work. An updated and simplified lithostratigraphic column for the Ajlun Group, based on the conclusions of this work, is presented in Fig. 11.

6.1.1. Sequence 1 and 2 (Base of sections to SB 2, majority of the Naur Formation)

These two sequences contain nannofossil zones CC 8, CC 9 and lowermost CC 10 and correspond to the majority of the Naur Formation (Fig. 7). Available $\delta^{13}C$ curves for this stratigraphic interval are restricted to W. Bustani and W. Mujib, with only the latter containing $\delta^{13}C$ data below SB 1. Consequently, this makes correlations difficult for most of this interval below SB 2. The positive $\delta^{13}C$ peak (+2.9 ‰) following SB 1 at ca. 69 m in W. Mujib may correspond to one of the three Lower Cenomanian Events (LCE) in the lower Cenomanian, identified in the English Chalk (Fig. 10) (Jarvis et al., 2006). A similar correlation could be established for the positive excursion (up to + 2.58 ‰) seen in W. Bustani at ca. 65 m, but remains challenging due to the insufficient data density within this interval. Intense dolomitization within the Naur Member b in W. Bustani (Fig. 7), furthermore restricted carbon isotope stratigraphy in the lower Naur Formation of this section.

Further upsection, a major positive excursion (labeled as 1 in brown color, Fig. 7) immediately below SB 2 (upper Naur Formation) is evident in W. Bustani (up to + 3.22 ‰ at ca. 90 m) and to a lesser extent in W. Mujib (up to + 2.1 ‰ at ca. 114 m). In W. Bustani, the base of this prominent excursion coincides with the lower/middle Cenomanian boundary set by the calcareous nannofossil CC 9/10 boundary and FO of the benthic foraminifera *Biplanata peneropliformis*, *Biconcava bentori*, *Pseudolituonella reicheli*, and *Praetaberina bingistani* at ca. 88 m (Messaoud et al., 2025). Although the base of this excursion is not resolved in W. Mujib, due to a data gap, the lower/middle Cenomanian boundary defined by the CC 9/10 boundary is located at ca. 105 m (Messaoud et al., 2025). Moreover, the occurrence of *Praealveolina tenuis* above ca. 115 m suggests a middle Cenomanian age (Philip et al., 1995; Bromhead et al., 2022). Analogous to W. Bustani, this strongly suggests that the base of this $\delta^{13}C$ excursion occurs in the interval between ca. 100–113 m in W. Mujib.

Similar to Jordan, a major positive carbon isotope excursion, with its base corresponding to the lower/middle Cenomanian boundary, is described for the English Chalk and represents the Mid Cenomanian Event (MCE) 1 (Jarvis et al., 2006). Given that the position of this major $\delta^{13}C$ excursion in W. Bustani and W. Mujib coincides with the lower/middle Cenomanian boundary, this peak is henceforth identified as the MCE 1 (Fig. 10). Analogous to its English Chalk counterpart, the MCE 1 in W. Bustani furthermore features two smaller, higher-order $\delta^{13}C$ peaks.

In W. Karak, a similar stratigraphic position for the MCE 1 near/below SB 2 is proposed by Wendler et al. (2014), although the peak itself is not shown in their data set given the limited stratigraphic extent of their $\delta^{13}C$ data (Fig. 7 and Appendix B). Nonetheless, this proposition is supported by their biostratigraphic constraints and the overall similarities between the different $\delta^{13}C$ curves post MCE 1 (Fig. 7).

6.1.2. Sequence 3 (SB 2 to SB 3, Fuheis and Karak/Hummar interval)

This sequence comprises the nannofossil zone CC 10 and corresponds to the Fuheis and Karak/Hummar lithostratigraphic interval (Fig. 7). It is characterized by two longer-term trends in its $\delta^{13}C$ curves in W. Karak and W. Mujib: a continued negative trend post-MCE 1, towards a $\delta^{13}C$ minimum and inflexion point (labeled in Roman numerals as I in brown color, Fig. 7), followed by rising $\delta^{13}C$ values towards SB 3. In W. Karak, the inflexion points from falling to rising $\delta^{13}C$ values occurs at ca. 152 m (ca. – 1.2 ‰) and in W. Mujib at ca. 155 m (-0.74 ‰), corresponding to the base of the *Neolobites vibrayeanus* zone in both sections (green zone, Fig. 7). Note that due to a gap (ca. 114–130 m) in $\delta^{13}C$ data points in W. Bustani, pinpointing this turnaround point is difficult, as the overall $\delta^{13}C$ trends cannot be described with the same certainty as with the examples above (Fig. 7).

A similar major inflection point, from falling to rising $\delta^{13}C$ values post MCE 1 in the lower middle Cenomanian, is reported in the English Chalk reference curve (Fig. 10) (Jarvis et al., 2006).

The long-term increasing $\delta^{13}C$ trend in the upper half of this sequence features at least two smaller-scale positive peaks (labeled as 2.1 and 2.2 respectively in brown color, Fig. 7) towards the upper Hummar Formation/Karak Member. Both of these $\delta^{13}C$ peaks are evident in W. Karak (ca. 155 and 162 m) and W. Mujib (ca. 160 and 173 m). These peaks likely occur in W. Bustani as well (ca. 132 and 142 m), although a significant data gap occurs within the marly interval below (ca. 113–130 m) introducing a degree of uncertainty when attempting to identify and correlate these smaller-scale events between the studied sections. Nonetheless, the overall rising carbon isotope trend towards SB 3 is evident in W. Bustani and similar to those seen in W. Karak and W. Mujib (Fig. 7).

Biostratigraphically, this interval with rising carbon isotope values in the upper Sequence 3 is set within nannozone CC 10 and furthermore includes the observed range of *Neolobites vibrayeanus* in W. Mujib (Nagm et al., 2017) and W. Karak (this study and also observed in Wendler et al. (2010; 2014), green ammonite zone, Fig. 7).

Despite the lack of ammonite biostratigraphy for the Karak Member in W. Bustani, the isotope correlations of this unit with the Karak Member in W. Karak and the Hummar Formation in W. Mujib can nonetheless be viable. This is due to the overall $\delta^{13}C$ curve similarities between the aforementioned sections as described above and the CC 10 nannofossil zone constraint within this Sequence 3 (Fig. 7).

This combination of ammonite stratigraphy (*Neolobites vibrayeanus* zone) and $\delta^{13}C$ curves showing similar long-term trends and short-term curve morphologies within Sequence 3 containing the Karak Member/Hummar Formation lithostratigraphic interval, verifies previous propositions (e.g., Schulze et al., 2003) that these separate lithostratigraphic units are indeed of coeval origin. Applying this concept, the commonly used F/H/S terminology, resulting from the difficulty in identifying the Hummar Formation south of W. Mujib could be resolved, by regarding the Karak Member as the lateral (southern) equivalent of the Hummar Formation. Hence, the Karak Member can be assumed as the dividing unit between the underlying Fuheis and the overlying Shueib formations south of W. Mujib (Fig. 11).

The middle/upper Cenomanian boundary in the English Chalk reference curve occurs at the Jukes Browne Event, which is characterized by a $\delta^{13}C$ maximum following the inflexion point from falling to rising carbon isotope values in the lower middle Cenomanian (Fig. 10) (Jarvis et al., 2006). It is biostratigraphically constrained by the transition from the *Acanthoceras jukesbrownei* to the *Calycoceras guerangeri* ammonite zone (Jarvis et al., 2006). Given the uncertainties in the precise downward stratigraphic range of *Neolobites vibrayeanus* (see Section 5.2), the identification of the Jukes Browne event in Jordan may be helpful to position the middle/upper Cenomanian boundary and overcome limitations of applying ammonite stratigraphy alone. In W. Mujib, the Jukes Browne event is tentatively placed in the upper Hummar Formation (*Neolobites vibrayeanus* zone) at ca. 173 m (peak 2.2, Fig. 10). At this position, $\delta^{13}C$ values reach a peak (ca. + 2 ‰), before falling to the base of the overlying OAE 2 $\delta^{13}C$ excursion, a long-term trend similar to the one described by Jarvis et al. (2006) (Fig. 10).

The resulting placement of the middle/upper Cenomanian boundary in W. Mujib would thus be higher than proposed by Messaoud et al. (2025), which sits at ca. 160 m in W. Mujib (compare Fig. 7 and Fig. 10). This proposed placement of the middle/upper Cenomanian boundary in the upper Hummar Formation, based on the Jukes Browne Event, would moreover be significantly higher than the position suggested by Nagm et al. (2017). Here, the authors place the boundary at the base of the Hummar Formation in W. Mujib, coinciding with the base of the *Neolobites vibrayeanus* range. Consequently, the current definition of the Jukes Browne Event would challenge a *Neolobites vibrayeanus* range constrained to the upper Cenomanian in Jordan and highlight a potential lower biostratigraphic range into the middle Cenomanian (Schulze et al., 2003; Wiese and Schulze, 2005). The placement of this event in W. Bustani (Fig. 10) is not possible due to the lack of sufficient carbon isotope data, although a correlation of the Jukes Browne event with peak 2.2 in W. Bustani cannot be excluded. In W. Karak, Wendler et al. (2014) place the event at ca. 162 m (peak 2.2, Fig. 10), supporting the placement of this event in W. Mujib.

6.1.3. Sequence 4 (SB 3 to SB 4, Shueib Formation)

This sequence comprises the nannofossil zones spanning the upper CC 10 and lower/middle CC 11 biozones and corresponds to the Shueib Formation (Fig. 7). Note the >30 m thickness increase in W. Karak compared to the surrounding sections in W. Bustani and W. Mujib within this sequence, reflecting additional accommodation space in the upper Cenomanian to lower Turonian in this area (Fig. 7, also see later in Section 6.2).

This interval begins with a long-term falling carbon isotope trend following the Jukes Browne $\delta^{13}C$ peak near/below SB 3 as described in the previous paragraph. A major turnaround towards rising values culminating in a prominent $\delta^{13}C$ excursion at the CTB (CC 10/11 boundary, lower blue line in Fig. 7 and 10) occurs within the marly intervals of the Shueib Formation in W. Karak, W. Mujib and W. Mukkawir and represents the OAE 2 (Jarvis et al., 2006; Wendler et al., 2014).

The OAE 2 excursion at the CTB is well expressed in W. Karak (up to ca. + 3.7 ‰ at ca. 190 m), W. Mujib (up to + 4.67 ‰ at ca. 200 m) and W. Mukkawir (up to + 3.51 ‰ at ca. 336 m) (grey zone, Fig. 7). The positioning of the OAE 2 carbon isotope event within the marly interval below the lower Turonian lower Walla Member in W. Mujib agrees with the OAE 2 position in W. Karak (Wendler et al., 2010, 2014). Interestingly, another chemostratigraphic study in the W. Karak section by Farouk et al. (2017) places the OAE 2 excursion within the Karak Member instead of the Shueib Formation, thus significantly below the placement of this study and Wendler et al. (2010, 2014). This differing definition of the OAE 2 is likely due to disputable biostratigraphic constraints and lithostratigraphic misinterpretations (e.g., identifying the uppermost Naur Member d as the Karak Member, see Section 5.1).

For the OAE 2 interval itself, the common three-part division into peak a, b and c described in W. Karak by Wendler et al. (2010, 2014) and in the English Chalk (Jarvis et al., 2006) is evident in W. Mujib and W. Mukkawir (Fig. 7 and 10). However, given a ca. 10 m thick data gap in W. Mujib, the exact uppermost extent of the OAE

2 excursion remains uncertain and can only be approximated and a minor hiatus cannot be excluded.

The approximate position of the OAE 2 in W. Bustani can be inferred from the CC 10/11 nannofossil boundary indicating the CTB as positioned by Messaoud et al. (2025) (lower blue line at ca. 168 m, Fig. 7). Moreover, this interval in W. Bustani coincides with a major nannofossil turnover zone, attributed to the apparent extreme environmental conditions at the CTB (blue stars in W. Bustani and W. Mujib, Fig. 7, Messaoud et al., 2025). Nannofossil turnover events at the CTB are globally recorded (Sooraj et al., 2024) and carbonate systems around the globe experienced a major faunal turnover and period of demise during this stratigraphic interval (Philip and Airaud-Crumiere, 1991; Schulze et al., 2004; Parente et al., 2008; Nagm et al., 2017; Valle et al., 2019; Bomou et al., 2020; Steuber et al., 2023; Philip et al., 2024; Petrizzo et al., 2025).

Measured $\delta^{13}C$ values for the inferred OAE 2 interval in W. Bustani were obtained from a marly interval featuring crosscutting secondary gypsum with extreme negative $\delta^{13}C$ values (up to – 8.41 ‰, see Appendix A), clearly reflecting a local diagenetic overprint. However, the negative $\delta^{13}C$ shift following SB 3 in W. Bustani at ca. 161 m could reflect the pre-OAE 2 negative $\delta^{13}C$ excursion seen in the other sections.

Following the OAE 2 excursion, the remaining part of Sequence 4 features two distinct $\delta^{13}C$ peaks (labeled as 3.1 and 3.2 in brown colors respectively, Fig. 7) corresponding to the lower and upper Walla Members respectively, before reaching extreme negative carbon isotope values at/around SB 4.

Here, the lower Walla is of particular interest, as its abundance of lower Turonian ammonites represents a key regional marker level (Schulze et al., 2003, 2005; Powell and Moh'd, 2011; Nagm et al., 2017) applicable to this work (orange zone, Fig. 7). The lower Turonian *Choffaticeras segne* zone in W. Mujib (Nagm et al. (2017) corresponds to the lower (peak 3.1) of the two distinct $\delta^{13}C$ excursions (+1.84 ‰ at ca. 219 m). Similarly, in W. Karak, the upper part of the lower Turonian *Choffaticeras* sp. Zone corresponds to peak 3.1 (ca. + 2.4 ‰ at ca. 222 m). Note that in Wendler et al. (2014), this peak occurs slightly above the ammonite bed due to slight (ca. <10 m) thickness differences between this and the aforementioned work (see Section 5.3.2 and Appendix B). The Walla Member in W. Bustani features an amalgamated carbonate cliff, separated by two thin (cm - dm scale) marl layers, corresponding to two carbon isotope peaks with +3.06 ‰ at ca. 181 m and +3.86 ‰ at ca. 195 m (Fig. 7). However, no diagnostic ammonites are documented within this interval. Nonetheless, the two carbon isotope peaks within the Walla Member in W. Bustani, could be correlated with the two $\delta^{13}C$ peaks observed in W. Karak and W. Mujib (see positioning of peaks 3.1 and 3.2 in the aforementioned sections, Fig. 7). Such a correlation is supported and constrained by the underlying CTB in W. Bustani defined by the CC 10/11 boundary below and the overlying shift to extreme negative $\delta^{13}C$ values near SB 4, a long-term $\delta^{13}C$ trend very similar to W. Karak and W. Mujib (Fig. 7). The Walla Member in W. Mukkawir is similarly composed on a singular carbonate cliff, however, given the lack of sufficient $\delta^{13}C$ data, no isotope correlation can be made.

The lower/middle Turonian boundary in the English Chalk reference curve is situated near the Lulworth Event. This event marks a significant inflexion point from long-term falling carbon isotope values following the OAE 2, to rising $\delta^{13}C$ values at the base of the *Collignoniceras woollgari* zone (Fig. 10) (Jarvis et al., 2006).

In Jordan, the upward stratigraphic limit of the lower Turonian *Choffaticeras segne*, found within the lower Walla Member, can be used as an approximation of the lower/middle Turonian boundary (Nagm et al., 2017). Applying this biostratigraphic constraint, the Lulworth Event in W. Mujib can be placed at the negative peak above the lower Turonian (Lower) Walla Member (labeled in Roman numerals as II in brown color, - 2.15 ‰ at ca. 225 m, Fig. 10). Such an approach is also consistent with the definition of this event in the English Chalk, as the proposed point signifies an inflexion point from long-term falling carbon isotope values post OAE 2, to rising carbon isotope values.

In W. Bustani, the Lulworth Event can tentatively be placed in the negative carbon isotope through (negative peak II, +0.80 ‰ at ca. 188 m, Fig. 10), separating the above described two carbon isotope peaks (3.1 and 3.2) within the Walla Member cliff. However, no long-term trends can be established due to the missing OAE 2 interval in W. Bustani. Moreover, the lack of ammonite constraints in this section, introduces further uncertainty in the placement of this carbon isotope event. Nonetheless, the placement of this event and thus the lower/middle Turonian boundary, is close to the chronostratigraphic boundary suggested by Messaoud et al. (2025), who place the boundary ca. 10 m above the proposed Lulworth Event of this work (compare this chronostratigraphic boundary for W. Bustani between Fig. 7 and 10).

Wendler et al. (2014) place the Lulworth Event in the lowermost part of the ammonite bearing lower Walla Member in their work in W. Karak, hence shifting their lower/middle Turonian boundary lower than proposed in this study (above the lower Walla Member). While their placement coincides with a major inflexion point from long-term falling to rising $\delta^{13}C$ values following the OAE 2, as described in the English Chalk curve (Fig. 10), it causes some disagreement with ammonite biostratigraphy. In both W. Karak and W. Mujib, much of the lower Walla Member ammonite fauna is characterized by lower Turonian fauna (Nagm et al., 2017). Given these discrepancies, the lower/middle Turonian placements in this study are henceforth tentative (Fig. 10).

The above-lying positive carbon isotope peaks in W. Karak (peak 3.2, ca. +3.1 ‰ at ca. 233 m) and W. Mujib (peak 3.2, +2.83 ‰ at ca. 228 m) are therefore constrained to the lower middle Turonian. In the English Chalk curve, a positive $\delta^{13}C$ excursion, named as Round Down, occurs in the lower middle Turonian, followed by a long-term fall in $\delta^{13}C$ values towards the upper middle Turonian (Fig. 10) (Jarvis et al., 2006). Hence, the positive $\delta^{13}C$ peak 3.2 in W. Mujib and W. Karak can therefore be correlated to the Round Down Event in the English Chalk (Fig. 10). Note that potentially higher $\delta^{13}C$ values directly above the Round Down Event placed as currently indicated in Fig. 10, cannot be ruled out, as a major zone of meteoric diagenesis/subaerial exposure associated with SB 4 occurs right above (red zone, Fig. 10). Contrary to the placement of the Round Down Event in this work at peak 3.2, Wendler et al. (2014) assign this event to the lower peak 3.1 (Fig. 10). While this approach is consistent with their proposed lower placement of the Lulworth Event and the lower/middle Turonian boundary (see discussion above), it creates significant disagreements with new biostratigraphic data (see discussion later this chapter). In W. Bustani, the identification of this event is challenging, given the earlier described lack of ammonite stratigraphic constraints and low data availability in the interval of interest.

All studied sections feature a drastic $\delta^{13}C$ shift to extreme negative values towards SB 4 (up to – 10.81 ‰ at ca. 244 m in W. Mujib). In W. Bustani, W. Karak, W. Mujib and to a lesser extent in W. Mukkawir, this interval corresponds to marine siliciclastics and supratidal deposits. Apart from obvious lithological influences on the $\delta^{13}C$ values not reflecting global DIC levels during deposition (e.g., evaporites or marine siliciclastics), meteoric influence within supratidal settings is also evident (e.g., desiccation cracks in W. Karak, Appendix E 2). Additionally, erosion below the marine siliciclastic interval in W. Bustani cannot be excluded (W. Bustani below ca. 208 m, Fig. 7).

These deposits highlight a major regional regression in Jordan and surrounding countries (Buchbinder et al., 2000; Bauer et al., 2003; Kuss et al., 2003; Schulze et al., 2003; Powell and Moh'd, 2011). Chronostratigraphic placements of these lowstand deposits at SB 4 are generally situated within the middle Turonian (Buchbinder et al., 2000; Bauer et al., 2003; Schulze et al., 2003; Wendler et al., 2014; Farouk et al., 2017; Messaoud et al., 2025), although lower Turonian ages have also been proposed (Powell and Moh'd, 2011). On the Arabian plate-scale, this regression marks the K150 SB (ca. 91.5 Ma) (Simmons et al., 2025), caused by a significant reconfiguration of the Arabian Plate's depositional systems following this major lowstand (Bromhead et al., 2022; Simmons et al., 2025). Despite clearly not reflecting global changes in the $\delta^{13}C$ of DIC in the world's oceans during times of deposition, the negative values at the K150 SB (SB 4) interval in Jordan nonetheless allow for regional and plate-wide correlations due to its synchronous regional occurrence during the middle Turonian (Fig. 7).

Significant differences in chronostratigraphic placements based on chemostratigraphy exist for the uppermost Shueib Formation (at SB 4) between this work and Wendler et al. (2014). While the negative $\delta^{13}C$ shift associated with the K150 SB in this work is attributed to regional factors resulting from the K150 SB, the aforementioned authors correlate this negative $\delta^{13}C$ event to the Southerham, Caburn and Bridgewick events occurring in the uppermost middle and lower upper Turonian in the English Chalk (Jarvis et al., 2006, 2015). This is disputable due to two main reasons. Firstly, as described earlier, the influence of lithology and meteoric diagenetic imprint (e.g., gypsum or desiccation cracks) occurring in this interval in W. Karak, strongly suggest that the deposits do not record the original global oceans $\delta^{13}C$ signal. Secondly, their biostratigraphic constraint for this interval (middle – upper Turonian CC 12 nannozone, Fig. 7) is challenged by the findings by Messaoud et al. (2025), who places the CC 12 zone significantly higher in the stratigraphy within the overlying Wadi as Sir Formation in W. Bustani and W. Mujib (Fig. 7). Instead, Messaoud et al. (2025) assign the uppermost Shueib Formation with SB 4 to the lower – middle Turonian CC 11 zone (see nannozones in W. Bustani and W. Mujib in Fig. 7). This is independently supported by the last appearance of the benthic foraminifera *Cuneolina pavonia parva?*, which suggests the placement of the middle/upper Turonian boundary in the W. Bustani section significantly higher (ca. below 330 m in the upper Wadi as Sir Formation, Fig. 7) (Whittaker et al., 1998; Messaoud et al., 2025).

6.1.4. Sequence 5 (SB 4 to SB 5, Wadi as Sir Formation)

This sequence features nannofossil zones CC 11 and CC 12 and corresponds to the Wadi as Sir Formation (Fig. 7). This stratigraphic interval reflects a full return to shallow water carbonate deposition post OAE 2 and the K150 SB. In the W. Bustani and W. Mujib sections, the long-term $\delta^{13}C$ fall following the Round Down Event (below SB 4) continues into the upper middle Turonian (CC 12 nannofossil zone), where an inflexion point (labeled in Roman numerals as III in brown color, Fig. 7 and 10) to rising values occurs in both sections. This negative peak III occurs with - 0.95 ‰ at ca. 290 m in W. Bustani and – 0.85 ‰ at ca. 302 m in W. Mujib (Fig. 7 and 10). A similar inflexion point from long-term falling to rising $\delta^{13}C$ values in the upper middle Turonian following the Round Down Event occurs in the English Chalk in form of the Glynde Event (Jarvis et al., 2006). Therefore, both of these negative $\delta^{13}C$ peaks (negative peaks III) in Jordan are correlated with the Glynde Event in the English Chalk (Fig. 10).

Intervals of (very) short, sudden negative $\delta^{13}C$ shifts occur in both sections around ca. 260 m in both sections respectively, with values as low as – 6.48 ‰ in W. Bustani (Fig. 7). As discussed above, such sudden shifts are likely the result of meteoric diagenesis. In W. Bustani, this is reinforced by a pack-to grainstone interval with abundant iron-rich exposure surfaces occurring within the same above-mentioned interval. Moreover, blocky calcite cements as well as common dissolution of aragonitic skeletal components are also observed from microfacies analysis at this level. Similarly, in

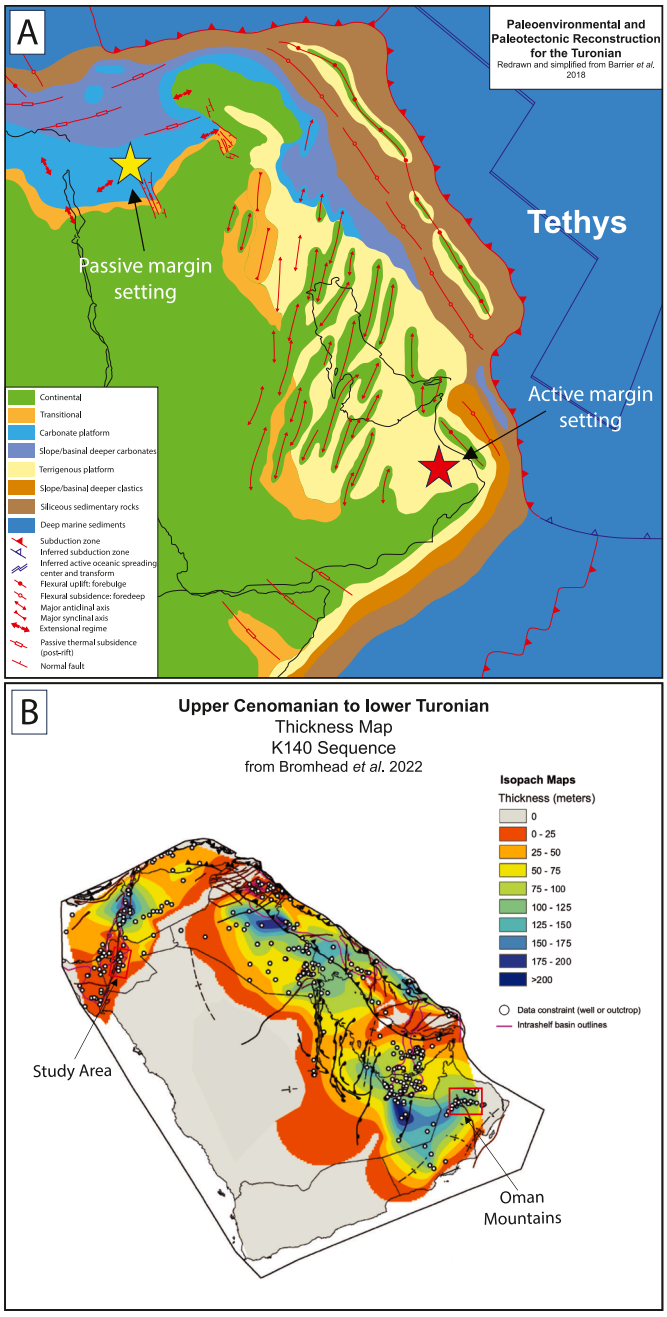

Fig. 12. A: Paleotectonic and paleoenvironmental reconstruction of the Arabian Plate during the Turonian, redrawn and edited from Barrier et al. (2018). Note the completed transition into an active margin and the foreland basin development on the eastern plate margin and the associated tectonic deformation structures, whereas the northwestern plate margin is marked by a largely passive margin environment. Also note the carbonate platform setting on the northwestern margin, whereas shallow water carbonate deposition has been completely halted on the eastern/northeastern margin. The yellow star marks the Levant Platform (study area of this work), while the red star marks the Oman Mountains. B: Isopach map of the Arabian Plate for the upper Cenomanian to lower Turonian from Bromhead et al. (2022). Note the different thicknesses between the Jordanian study area of this work and the Oman Mountains, outlined in red rectangles on each plate margin.

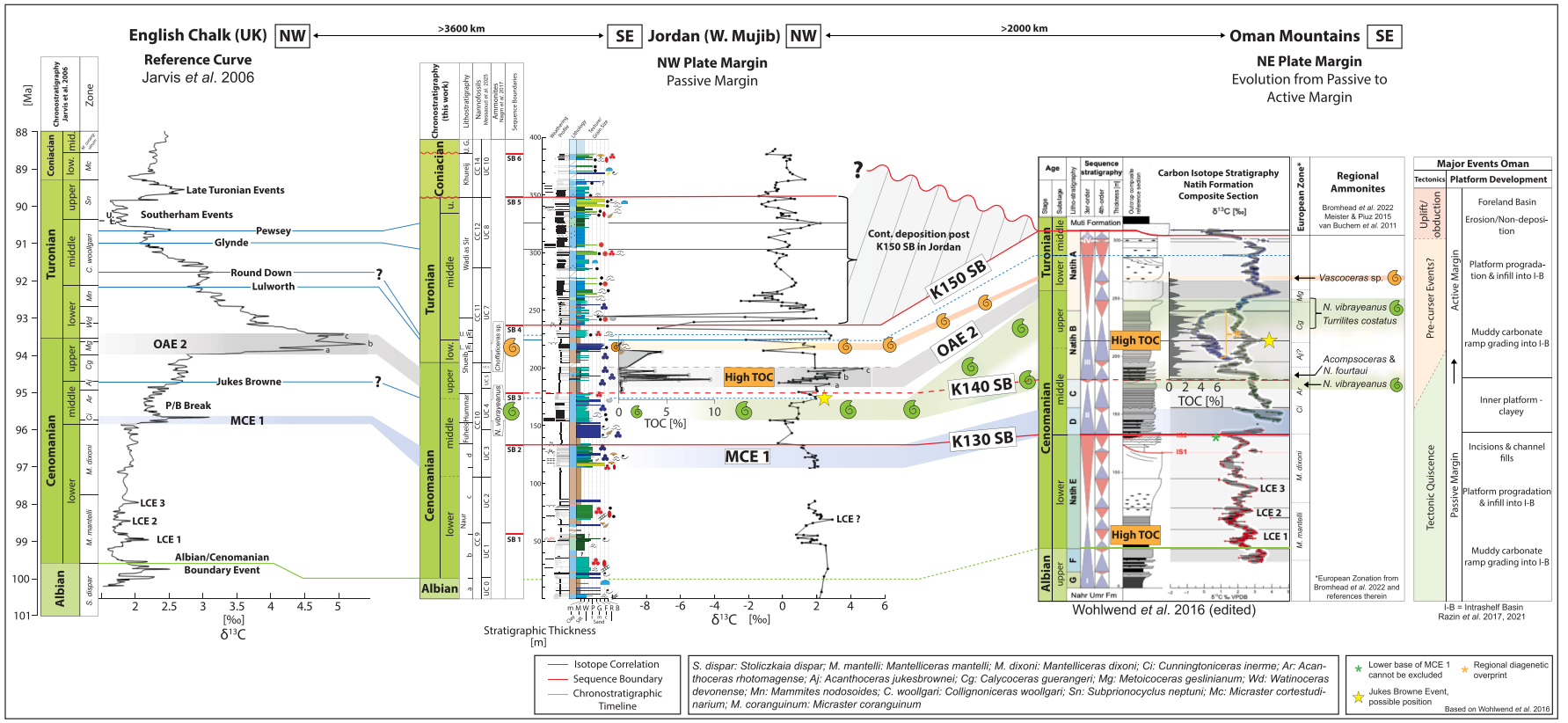

Fig. 13. Plate-wide high-resolution correlation between Jordan and the Oman Mountains (Natih Formation). The Arabian curves are furthermore correlated with the English Chalk (UK) reference curve. The carbon isotope curve from Oman is obtained from Wohlwend et al. (2016), while the English Chalk curve is reproduced from Jarvis et al. (2006). Abbreviations of lithostratigraphic units: L. W.: Lower Walla Member, U. W.: Upper Walla Member and U.G.: Umm Ghudran Formation. For legend for the W. Mujib log, see Fig. 7.

W. Mujib, the interval around ca. 260 m features intense coarse crystalline dolomitization, hinting towards significant diagenetic overprint. While such findings indicative of meteoric diagenesis highlight the drawback of using shallow water carbonates as a carbon isotope record, the local and stratigraphically concentrated occurrence of such intervals does not pose a major drawback.

Maximum long-term $\delta^{13}C$ values (labeled as 4 in brown color in Fig. 7 and 10) in the upper part of Sequence 5 occur in W. Bustani (+2.96 ‰ at ca. 320 m) and W. Mujib (+2.20 ‰ at ca. 325 m), followed by falling carbon isotope values towards SB 5 (Fig. 7 and 10). This peak likely occurs within the upper middle Turonian, as the last appearance datum of the middle Turonian benthic foraminifera *Cuneolina pavonia parva?* (interpreted to mark the middle/upper Turonian boundary (Whittaker et al., 1998; Messaoud et al., 2025) occurs above this peak in W. Bustani at ca. 330 m. Hence, this peak and the equivalent peak in W. Mujib can likely be correlated with the Pewsey Event in the English Chalk, featuring a similar long-term carbon isotope trend and chronostratigraphic position within the upper middle Turonian (Fig. 10) (Jarvis et al., 2006).

In W. Mujib, the short-term carbon isotope peak (+0.75 ‰ ca. 335 m) between the underlying Pewsey $\delta^{13}C$ event (Peak 4) and SB 5 above, is set at the suggested middle/upper Turonian boundary defined by Messaoud et al. (2025) (Fig. 10). Based on this biostratigraphic constraint, this short-lived positive peak could represent one of the Southerham Events described at the middle/upper Turonian boundary in the English Chalk by (Fig. 10) Jarvis et al. (2006). The stratigraphic position of the Southerham Events in Jordan as proposed in this work, sits significantly higher than the position advocated by Wendler et al. (2014) who placed it within the uppermost Shueib Formation (see discussion above).

A significant >400 ka hiatus is identified in the W. Bustani and W. Mujib sections by the absence of the CC 13 nannofossil zone by Messaoud et al. (2025) at the top of the Wadi as Sir Formation marking SB 5 (Fig. 7 and 10). A sudden (>+2 ‰ magnitude) isotopic shift at SB 5 can be observed in W. Bustani, indicating a break in sedimentation, while the $\delta^{13}C$ in W. Mujib shows a more subtle negative shift (Fig. 7). The latter example underscores the importance of integrating $\delta^{13}C$ data with biostratigraphic constraints, as this hiatus would have been likely missed if relying solely on carbon isotope chemostratigraphy.

6.1.5. Sequence 6 (SB 5 to SB 6, Khureij Formation)

This sequence comprises the nannofossil zone CC 14 and corresponds to the Khureij Formation, which has been identified in all logged sections (Fig. 7). This sequence only contains sufficient $\delta^{13}C$ data in W. Mujib (Fig. 7). However, given the low-resolution biostratigraphic constraints for the Coniacian in this interval (Messaoud et al., 2025), a global correlation with the reference curve from the English Chalk is difficult to establish. The relatively sudden negative $\delta^{13}C$ shift at SB 6 in W. Mujib (ca. 385 m, Fig. 7) reflects the sudden lithology change from limestone to overlying chalk and a possible hiatus due to Coniacian platform drowning, terminating the deposition of the Ajlun Group (Powell and Moh'd, 2011).

6.2. Plate-wide correlation: impact of tectonics on sequence stratigraphic evolution on the Arabian Plate

The Jordan age model presented in this work provides a new reference point for the northwestern plate margin, allowing for high-resolution stratigraphic correlations across the Arabian Plate for the Cenomanian to Turonian interval. Such a reference point is essential, as the northeastern and eastern margins of the Arabian Plate saw the transition from a passive to an active margin during the Cenomanian to Turonian interval, whereas the northwestern margin remained in a largely passive margin setting (Fig. 12A) (e.g., Barrier et al., 2018). The resulting effects of this transition on carbonate deposition were profound and varied across the plate and are recorded in form of the mid-Turonian K150 SB across the Arabian Plate (Simmons et al., 2025). Significant differences exist in the impact of this SB on carbonate deposition, with a quick reestablishment of shallow water carbonate production following this event on the northwestern margin, while large parts of the northeastern and eastern margins saw the termination of carbonate sedimentation, significant erosion and the deposition of deeper marine marls and clays (Bromhead et al., 2022 and references therein; Powell and Moh'd, 2011). Of interest here is the suggestion, that tectonic precursor events may have affected sedimentation preceding the main phase of uplift in the Turonian (Simmons et al., 2025). A comparison between the new high-resolution data set in Jordan and well-established age models from Oman on the eastern plate margin may help to unravel this.

In Oman, the upper Albian to lower Turonian Natih Formation is largely composed of carbonate platform deposits. Exposed in the Oman Mountains (Fig 12A), the Natih Formation is subdivided into seven members (A to G from top to base) and features three large-scale depositional sequences (Sequences I-III, Fig. 13) (e.g., van Buchem et al., 2002; Razin et al., 2017). It has been studied extensively in both outcrop and subsurface in terms of its sedimentology and sequence stratigraphic architecture (van Buchem et al., 1996, 2002, 2011; Grélaud et al., 2006, 2010; Droste, 2010; Razin et al., 2017), biostratigraphy (e.g., Meister and Piuz, 2015; Vicedo and Piuz, 2017) and chemostratigraphy (Vahrenkamp, 2013; Wohlwend et al., 2016). An extensive overview on the age dating of the Natih Formation is furthermore provided in Bromhead et al. (2022). As such, the Natih Formation provides the ideal reference point for the following plate-scale correlation between the northwestern (Jordan) and the eastern (Oman) plate margins.

Figure 13 shows the correlations between Jordan and Oman, constrained by chemo- and biostratigraphic age constraints (see references in Fig. 13) and sequence boundaries after van Buchem et al. (1996, 2002, 2011) as described in Bromhead et al. (2022). The stratigraphic section in Jordan represents a carbonate shelf setting (W. Mujib), while the Natih Formation in Oman is represented by a summary profile from Wohlwend et al. (2016) based on Grélaud et al. (2010) and is situated in a comparable shelf setting. The $\delta^{13}C$ curve from Oman is obtained from Wohlwend et al. (2016) and biostratigraphic ranges of key regional ammonites as well as the European ammonite zones are from van Buchem et al. (2011), Meister and Piuz (2015) and Bromhead et al. (2022) and references therein.

6.2.1. Uppermost Albian to MCE 1 (lower/middle Cenomanian boundary)

The first interval from the uppermost Albian to the MCE 1 (at the lower/middle Cenomanian boundary) features comparable thicknesses of ca. 100 m between Jordan and Oman and covers Naur Formation and the Natih G to E respectively (Fig. 13). In Jordan, the Albian to Cenomanian transition is defined biostratigraphically (Messaoud et al., 2025), whereas in Oman, the Albian/Cenomanian Boundary Event is also recognized from $\delta^{13}C$ data, apart from biostratigraphic markers (Bromhead et al., 2022). As discussed previously, correlations between the different LCE is challenging (see Section 6.1), due to a lack of available carbon isotope datapoints in Jordan. The top of this interval, the lower/middle Cenomanian transition, is well-established in Jordan (uppermost Naur Formation) and Oman (Top Natih E), by means of chemostratigraphy (MCE 1, blue zone in Fig. 13) and biostratigraphic constrains (Bromhead et al., 2022; Messaoud et al., 2025). Note that

a slightly lower position of the lower/middle Cenomanian boundary within the uppermost Natih E in Oman cannot be excluded (Wohlwend et al., 2016 and references therein). A major SB occurs near the lower/middle Cenomanian boundary and the MCE 1 zone in both Jordan (SB 2) and Oman (top of Sequence 1, Fig. 13), associated with the K 130 SB (Sharland et al., 2001; Bromhead et al., 2022). A eustatic sea level fall at this stratigraphic interval is suggested, with an estimated magnitude of up to ca. 20–30 m in Oman, inferred from channel incisions on top of the Natih E at the K 130 SB (van Buchem et al., 1996, 2002; Grélaud et al., 2006; 2010) (IS 1 and 2 in Fig. 13). In Jordan, the major regional SB 2 is evident in the uppermost Naur Formation from a prominent sharp surface terminating a regressive trend throughout most of the upper Naur. In the studied transect, reflecting an inner platform setting (Fig. 1A), no equivalent incisions on the magnitude of the Omani incisions are observed. Locally, minor (m-scale) erosive features occur at SB 2 in southern Jordan (Ras en Naqb, Fig. 1A), while the uppermost Naur Formation in central Jordan features prograding clinoforms with erosive tops (Al-Haydan near W. Mujib). Despite this difference in the expression of the K130 SB, the relative isopach nature of this uppermost Albian to lower/middle Cenomanian interval (Fig. 13), suggests a predominant eustatic control on both sides of the Arabian Plate, which is supported by a lack of structural deformation visible from this time in Oman (Grélaud et al., 2006). A notable difference exists in the preservation of organic matter-rich sediments between Oman and Jordan in the lower Cenomanian, where shales rich in TOC are located in intrashelf basin deposits of the Natih E (van Buchem et al., 1996, 2002), whereas the Jordanian sections show no comparable TOC occurrences within their shallow water carbonate platform settings (Fig. 13).

6.2.2. MCE 1 (lower/middle Cenomanian boundary) to OAE 2 (Cenomanian/Turonian boundary)

The interval spanning the MCE 1 (lower/middle Cenomanian boundary) to the OAE 2 (Cenomanian/Turonian boundary), largely covers the Fuheis, Hummar and Shueib formations in Jordan and the Natih D, C, B and lower A members in Oman (Fig. 13). As shown in Fig. 13, both events are well established by their respective prominent carbon isotope excursions and are furthermore well controlled by biostratigraphic constraints in both locations (this study and Wohlwend et al. (2016)). Consequently, both the MCE 1 and OAE 2 provide two solid stratigraphic anchor points for long-range correlations across the Arabian Plate.

Measuring from the top of the MCE 1 to the base of the OAE 2, the correlation between W. Mujib and Oman for this interval features notable thickness differences, with the latter one showing ca. 40 m of additional thickness and hence accommodation space (Fig. 13). It must be noted, that slight to moderate thickness variations of several 10's m also depend on the position on the respective carbonate platform, as proximal-distal trends and basin-swell morphologies can affect measured thicknesses within a basin as observed in Jordan (Schulze et al., 2003). This can be seen in the studied transect of this work as well, where the more distal W. Mukkawir features 10's m of additional thickness throughout most of the Ajlun stratigraphy compared to its more proximal counterparts (Fig. 7). Moreover, the more proximal W. Karak section features a slight, >10 m, increase in thickness compared to W. Mujib for the stratigraphic interval from the top of the MCE 1 to the base of the OAE 2 (Fig. 7). This slight thickness variation likely reflects the beginning development of a regional intrashelf basin covering the W. Karak area (see later this section).

The Oman-Jordan correlation before the MCE 1 features remarkably similar thicknesses (see above), before the aforementioned increase in stratigraphic thickness in the interval between the MCE 1 and OAE 2 occurs. This suggests, that the increased rates of accommodation creation started during the middle to late Cenomanian and are not due to different positions of the studied sections on their respective platforms, for example reflecting a proximal-distal trend. An overall increased accommodation space creation in Oman compared to Jordan is furthermore also supported by upper Cenomanian to lower Turonian isopach maps from Bromhead et al. (2022) (Fig. 12B). The causes for this middle to upper Cenomanian increase in accommodation space creation on the eastern margin, compared to Jordan, could be explained by tectonic precursor events related to the subduction of the Neo-Tethys, which commenced in the Cenomanian (Simmons et al., 2025). Applying the age constraints from the discussion above, along with the observation of increased accommodation space creation in Oman beginning in the middle to late Cenomanian time interval, allows for a more precise timeframe for the onset of said precursor events. As such, the initiation of precursor events affecting the sedimentation patterns in the Oman Mountains can be narrowed down to this same stratigraphic interval. Thus, based on the correlation presented in Fig. 13, the transition from a passive to an active margin might already have occurred during the middle to late Cenomanian interval in the Oman Mountains.

Contrary to this, the northwestern Arabian Plate margin saw no comparable, regional-scale tectonic forcings during the Cenomanian to Turonian interval and remained largely passive (Barrier et al., 2018). As mentioned earlier (Section 2), local tectonic influence on sedimentation patterns as early as during the late Cenomanian have been inferred in the Sinai and Israel, based on significant stratigraphic hiatuses occurring on paleo-highs during the CTB interval as well as stratal thinning patterns (Buchbinder et al., 2000; Bauer et al., 2003). These tectonically forced sedimentation patterns on the Sinai Microplate (Fig. 1A) might reflect an early onset of intraplate deformation linked to the Syrian Arc formation (e.g., Bauer et al., 2003). On the other side of the DST, no comparable tectonic influences in the Jordanian study area can be inferred from our stratigraphic data (Fig. 7) and previous outcrop (Schulze et al., 2003; Powell and Moh'd, 2011; Messaoud et al., 2025) and subsurface studies (Kalifi et al., 2025). However, given the geographic and temporal (late Cenomanian) proximity to the above-described tectonic events in the Sinai and Israel, a potential tectonic component in the formation of the Jordanian depocenter in the W. Karak area could be relevant. Nonetheless, the overall regional tectonic setting in the study area in Jordan is marked by a largely passive margin, clearly contrasting the situation on the eastern margin in Oman with the transition into an active margin environment.

Such an early onset of tectonic precursor events in Oman could furthermore implicate a potential tectonic component in the formation of the organic-rich Natih B intrashelf basins. Previously, the formation of these intrashelf basins has been assumed to be controlled by local environmental factors resulting in differential aggradation, in turn leading to the formation of intrashelf basin topography (van Buchem et al., 2002; Razin et al., 2017). Given the aforementioned suggested early onset of tectonic influence during the middle to late Cenomanian (Post-MCE 1 to OAE 2, Fig. 13) in Oman, a tectonic contribution to the formation of the Natih B intrashelf basins cannot be ruled out.

Situated between the aforementioned lower (MCE 1) and upper (OAE 2) stratigraphic anchor points, the well-established plate-scale K140 SB described for Oman (van Buchem et al., 2011; Bromhead et al., 2022), presents some challenges when attempting to correlate it with the regional SB 3 in Jordan (Fig. 13). These largely stem from conflicting positionings of the middle/upper Cenomanian boundaries between different authors in Oman (van Buchem et al., 2011; Wohlwend et al., 2016; Bromhead et al., 2022), as correlating the K140 SB in Oman with SB 3 in Jordan

would cross the differing middle/upper Cenomanian boundaries (Red dashed line, Fig. 13). Note that disagreements in the positioning of this chronostratigraphic boundary in Jordan exist as well within the Hummar Formation (see Section 6.1). However, any alternative position of the middle/upper Cenomanian boundary within the Hummar Formation in W. Mujib, as proposed by other authors, would still pose a significant problem when correlating SB 3 to the K 140 SB in Oman, as the direct correlation between both sequence boundaries would still cross the chronostratigraphic middle/upper Cenomanian boundary. The definition of the middle/upper Cenomanian boundary in Oman is more uncertain, with ammonites generally assigned to an upper Cenomanian stratigraphic range (e.g., *Neolobites vibrayeanus*, Wiese and Schulze, 2005) occurring within the upper Natih C (van Buchem et al., 2011) (see lower extent of the *Neolobites vibrayeanus* range in Fig. 13). Newer biostratigraphic works report middle Cenomanian ammonites higher up within the lower Natih B (e.g., *Neolobites fourtaui* and *Acompsoceras*) and younger fauna (e.g., *Neolobites vibrayeanus*) in the overlying upper Natih B strata, hence proposing a middle/upper Cenomanian transition within the Natih B (Meister and Piuz, 2015).

Additionally, chemostratigraphic work by Wohlwend et al. (2016) propose the position of the Jukes Browne $\delta^{13}C$ event within the Natih B (yellow star, Fig. 13), marking the middle/upper Cenomanian transition in the English Chalk (Jarvis et al., 2006). This placement is supported by the ammonite stratigraphy described above (Meister and Piuz, 2015).

In Oman, the position of this transition could be further supported by a direct comparison of both $\delta^{13}C$ curves from Jordan and Oman shown in Fig. 13. Taking the well-established MCE 1 and the OAE 2 as lower and upper chemostratigraphic anchor points respectively, the comparison of both curves within this interval shows a remarkably high degree of similarity. Starting at the top of the MCE 1 (blue zone, Fig. 13), both curves feature a long-term trend towards a $\delta^{13}C$ minimum occurring directly at the base of the Hummar Formation in Jordan and the lowermost Natih B in Oman. This is followed by a rise to more positive $\delta^{13}C$ values with two higher-order positive peaks within the Hummar and the Natih B respectively. Here, the upper one of these positive peaks (yellow stars) are interpreted as the Jukes Browne Event in this work (see Section 6.1) and by Wohlwend et al. (2016) in Oman. This trend is followed by a short-term negative carbon isotope shift in both locations, succeeded by the $\delta^{13}C$ rise towards the OAE 2 (upper anchor point). However, the above-mentioned different accommodation spaces between Oman and Jordan, in effect vertically stretching the carbon isotope profile within the interval of interest, could potentially introduce a source of error when correlating the carbon isotope curves between both regions within this specific interval between the MCE 1 and OAE 2. Additionally, the nature of the Omani curve being a composite curve and local diagenetic effects could introduce another potential source of error (see the prominent negative excursion in the blue carbon isotope curve within the Natih B, attributed to local diagenetic effects, Wohlwend et al., 2016, Fig. 13).

Nevertheless, while higher resolution correlations between the well-established MCE 1 and OAE 2 highlight the conflicting correlations between sequence-, bio- and chemostratigraphy, this does not question the correlations between the aforementioned carbon isotope events between Jordan and Oman. As mentioned in the beginning of the discussion for this interval, the Omani sections clearly show an increased accommodation space creation (10's m) beginning during the middle to late Cenomanian interval, potentially reflecting the onset of tectonic precursor events marking the shift from a passive to an active margin on the eastern Arabian Plate. A slight diachronous nature of the expression of the K140 SB on both sides of the Arabian Plate, >2000 km apart, may have to be considered, likely caused by the tectonic overprint along the Oman margin at that time.

6.2.3. Post-OAE 2 (Cenomanian/Turonian boundary) to K150 SB (middle Turonian)

Correlations for the post OAE 2 interval are based on ammonites and carbon isotope data. The occurrence of the upper Cenomanian to lower Turonian ammonite genus *Vascoceras* (orange zone, Fig. 13) above the OAE 2 interval indicates a lower Turonian stratigraphic placement (Meister and Piuz, 2015; Nagm et al., 2017). A negative $\delta^{13}C$ peak within the Natih A could represent the Lulworth carbon isotope Event shown in W. Mujib (blue dashed line) and occurring at the lower/middle Turonian transition (Jarvis et al., 2006). This middle Turonian placement of the uppermost Natih A is also in agreement with Wohlwend et al. (2016).

While the onset of tectonic precursor events in Oman potentially began during the middle to late Cenomanian as discussed above, the main uplift and obduction is dated to the middle Turonian, highlighted by a tectonically forced regressive trend within the Natih A and finally the K150 SB (Razin et al., 2017; Simmons et al., 2025). In Oman, this now completed transition from a passive to an active margin resulted in widespread erosion of underlying strata and the formation of incised valley system associated with the K150 SB on top of the Natih Formation (Razin et al., 2017). Over time, the development of a forebulge basin resulted in the complete stop in shallow water carbonate production on the eastern plate margin and the deposition of the deeper water marls of the Fiqa and Muti formations (Razin et al., 2017; Bromhead et al., 2022; Simmons et al., 2025). Contrary to this, the largely passive northwestern plate margin was also marked by the middle Turonian K150 SB as evident from the siliciclastic and supratidal deposits in Jordan and its surrounding countries (see Section 6.1). While incisions of up to ca. 20 m do exist locally in southern Jordan (Ras en Naqb), no widespread regional-scale erosion or extensive incised valley systems exist within the study area of this work. More importantly, the shallow water carbonate factory saw a complete return post-K150 SB, as evident in the >100 m thick shallow water carbonates of the Wadi as Sir Formation (Powell and Moh'd, 2011). These key differences highlight the obvious dominant tectonic influence in the east and suggest a stronger eustatic component in the K150 SB on the northwestern plate margin (Simmons et al., 2025). As discussed by these authors, a coeval drop in eustatic sea level does occur and is likely the dominant factor for the sequence boundary in Jordan, whereas in Oman, this drop in global sea level enhanced the tectonic uplift during the middle Turonian.

6.2.4. Lateral and temporal trends in the distribution of organic-rich sediments

The diachronous occurrence of organic-rich facies in the upper Cenomanian to lower Turonian interval between both regions is shown in Fig. 13. In Jordan, high-TOC values are clearly associated with the OAE 2, whereas in Oman, the high-TOC facies occurs before the OAE 2 in association with the Natih B intrashelf basin development (Vahrenkamp, 2013; Wohlwend et al., 2016). The Natih B intrashelf basins, containing the high-TOC deposits, are linked to the transgressive phase (Sequence III, Fig. 13), where differential sedimentation rates resulted in the creation of intrashelf basin topography, necessary for the accumulation and preservation of organic matter (van Buchem et al., 2002, 2005). Similarly, Wohlwend et al. (2016) argue that the timing of TOC deposition in Oman was controlled by restriction from the Neo-Tethys Ocean, resulting from the development of intrashelf basins during the Natih B interval.

Interestingly, the Cenomanian to lower Turonian Shilaif intrashelf basin in the adjacent UAE features two distinct high-TOC occurrences within the same basin: here, a first increase in TOC concentrations occurs before the OAE 2, similar to Oman as outlined above, while a second spike is recorded in a more basinward position during the OAE 2 excursion (Hennhoefer et al., 2020). Analogous to the example in Oman, the authors attribute the temporal and spatial variation in organic matter-rich sediment occurrence to bathymetric differences and varying degrees of restriction to the open ocean.

On the northwestern plate margin on the Levant Platform, upper Cenomanian to lower Turonian intrashelf basins are reported in Jordan (Karak-Silla Basin) as well as further southwards in Egypt (Central Sinai Basin) and Israel (Eshet Zenifim Basin) and likely represent a continuous paleo-geographic depression (Buchbinder et al., 2000; Bauer et al., 2003; Schulze et al., 2005). In the studied transect, the basinal parts are inferred for the W. Karak and W. Mukkawir area, while W. Mujib is interpreted as a paleo-high during the late Cenomanian to early Turonian (Schulze et al., 2005). As mentioned earlier in Section 6.1, such a paleo-topographic interpretation following the upper Cenomanian is supported by the thickness trends shown in Fig. 7, where the W. Karak section shows increased thickness relative to its surrounding sections.

Several areas of restricted-dysoxic environments are proposed to occur during the CTB interval within the intrashelf basin in the studied area of this work by Schulze et al. (2005). These include the areas covered by the W. Karak and W. Mukkawir sections. While low oxygen seafloor conditions can be inferred for the W. Karak section based on a significant TOC accumulation (up to ca. 3 wt.-%, Fig. 7) in the studied sediments for the OAE 2 interval (Wendler et al., 2014), no comparable concentrations can be observed in the W. Mukkawir section within the OAE 2 excursion (up to ca. 0.5 wt.-%, Fig. 7). Moreover, despite W. Mujib representing a slight paleo-high structure in the transect shown in Fig. 7 and in previous work by Schulze et al. (2005), the CTB interval in this section features the highest TOC concentrations measured in the study area (up to 9.5 wt.-%). Such a stark increase in TOC likely reflects increased oxygen deficiency and/or increased primary productivity in the W. Mujib area, occurring during the CTB.

Consequently, these findings suggest that the control on the deposition and preservation of organic-rich sediments during the OAE 2 cannot be explained by thickness variations alone, as one would expect to see higher TOC concentrations within the deeper W. Karak and W. Mukkawir sections compared to W. Mujib sitting on an apparent paleo-high. Here, other paleoenvironmental factors such as the connection to the open ocean or proximity to detrital sources, in turn influencing the lateral and temporal variations in paleo-redox conditions or paleo-primary productivity need to be taken into account (e.g., Wang et al., 2023). Nonetheless, the coeval occurrence of high-TOC facies with the OAE 2 strongly suggests that the timing of organic-rich facies deposition was primarily controlled by global factors related to the OAE 2 in Jordan, whereas in Oman, local/regional factors seem to have "overridden" the global signals (Wohlwend et al., 2016).

7. Conclusion

The present work is based on four complete sedimentary sections of the uppermost Albian to Coniacian aged Ajlun Group in western Jordan. New $\delta^{13}C$ curves for three sections are combined with previously published carbon isotope data (Wendler et al., 2014) and constrained by macro- and micropaleontological biostratigraphic information from this study and previous works (Nagm et al., 2017; Messaoud et al., 2025) within an overall sequence stratigraphic framework (SB 1–6). Several carbon isotope events are identified in the Jordanian basin by correlations with a global reference curve in the UK (Jarvis et al., 2006) including the MCE 1, OAE 2 and the Pewsey events. The new findings build a new high-resolution age model for the Jordanian Ajlun Group and have several local implications:

- The results highlight the power of a multi-proxy stratigraphic approach as a basin-wide correlation tool, which helps to resolve stratigraphic discrepancies, such as the demonstration of the time-equivalence of the Karak Member (Fuheis Formation) and the Hummar Formation. Such correlations provide the basis for future sequence stratigraphic models of the Jordanian Ajlun Group.
- The present work offers a stratigraphically extended carbon isotope record covering most of the Ajlun Group, including the significant >100 m thick Turonian Wadi as Sir Formation, while earlier studies focused around the Fuheis/Hummar/Shueib interval and the CTB. Moreover, the results of this work mostly support previous chemostratigraphic placements, however, also find discrepancies resulting from unclear lithostratigraphic definitions and disputable biostratigraphic constraints. These discussions highlight the importance of using carbon isotope analysis with suitable constraints.

On a regional plate-wide scale, the new $\delta^{13}C$ data, in integration with the aforementioned sedimentological and biostratigraphic works, represents a new (chemo-) stratigraphic anchor point for the northwestern Arabian Plate margin for the Cenomanian to Turonian interval. High-resolution correlations of 3rd order sequences between Jordan (passive northwestern margin) and the Natih Formation in Oman (eastern margin evolving from a passive to an active margin) allow for evaluating the relative influences of eustacy against tectonics on both margins. Correlations show increased thickness (ca. 40 m) and hence accommodation space in Oman compared to Jordan, within the interval spanning the top of the MCE 1 to the base of the OAE 2. These results suggest the onset of tectonic precursor events (associated with the closing of the Neo-Tethys Ocean) affecting accommodation space creation in the Oman Mountains during the middle to late Cenomanian interval. This precedes the main phase of uplift and erosion occurring during the middle Turonian (expressed in the K 150 SB) and advocates that the transition from a passive to an active margin began earlier during the middle to late Cenomanian interval. Additionally, such an early onset of precursor events introduces the possibility, that the formation of the organic-rich Natih B intrashelf basins during middle Cenomanian might have had a tectonic component.

The absence of high TOC facies in Oman within the OAE 2 interval contrasts TOC concentrations up to 9.5 wt.-% in Jordan (W. Mujib) occurring during the OAE 2. This temporal discrepancy in the deposition and preservation of organic-rich sediments between both sides of the Arabian Plate, suggests that the deposition and preservation of such sediments was primarily controlled by global factors associated with the OAE 2 in Jordan, whereas in Oman, regional factors overrode the global factors (Wohlwend et al., 2016).

However, as seen in the Jordanian transect of this work, significant local lateral variations in TOC concentrations occur also on an intrabasinal scale during the OAE 2 interval. Such variations imply that local factors influencing the preservation of organic-

rich facies must also be taken into account in future works by applying geochemical proxies investigating paleoenvironmental factors (e.g., paleo-productivity, redox conditions, detrital influx).

CRediT authorship contribution statement

Tojo Chirakal: Writing – review & editing, Writing – original draft, Visualization, Methodology, Investigation, Data curation, Conceptualization. **Jihede Haj Messaoud:** Writing – review & editing, Data curation. **Ali Alibrahim:** Writing – review & editing, Data curation. **Khalil Ibrahim:** Writing – review & editing, Data curation. **Carine Grélaud:** Writing – review & editing, Data curation. **Amir Kalifi:** Writing – review & editing, Data curation. **John H. Powell:** Writing – review & editing, Data curation. **Frans van Buchem:** Writing – review & editing, Supervision, Project administration, Funding acquisition, Data curation.

Funding sources

This study was funded by the King Abdullah University of Science & Technology baseline support of Principal Investigator Frans van Buchem.

Declaration of competing interest

The authors declare that they have no known competing financial interests or personal relationships that could have appeared to influence the work reported in this paper.

Acknowledgements

We thank King Abdullah University of Science & Technology (KAUST) laboratory staff member Elhadj Marwane Diallo for his assistance in running the RockEval measurements and Yuriy Kaprielov for his assistance in digitizing our figures. Furthermore, we acknowledge the Hashemite University (Amman, Jordan) for their logistical support during field work. We also thank the two anonymous reviewers for their constructive criticism, suggestions and assistance in improving our original manuscript. John H. Powell publishes with the permission of the Director, British Geological Survey (NERC).

Data availability

Data will be made available on request.

References

Abu Saad, I., Andrews, I.J., 1993. A database of stratigraphic information from deep boreholes in Jordan, Subsurface Geology Bulletin 6. Geology Directorate. Subsurface Geology Division, Ministry of Energy and Mineral Resources, NRA, Amman, Jordan.

Al Hseinat, M., AlZidaneen, M., Jaradat, R., Al-Rawabdeh, A., Hübscher, C., 2023. Tectono-stratigraphic framework and evolution of the northwestern Arabian plate, Central Jordan. Tectonophysics 863, 229993. https://doi.org/10.1016/j.tecto.2023.229993.

Allan, J.R., Matthews, R.K., 1982. Isotope signatures associated with early meteoric diagenesis. Sedimentology 29, 797–817. https://doi.org/10.1111/j.1365-3091.1982.tb00085.x.

Aly, M.F., Smadi, A., Abu Azzam, H., 2008. Late Cenomanian-Early Turonian ammonites of Jordan. Revue de Paléobiologie 27, 43–71.

Andrews, I.J., 1992. Cretaceous and Paleogene lithostratigraphy in the subsurface of Jordan, Subsurface Geology Bulletin. Geology Directorate, Subsurface Geology Directorate, NRA, Jordan 5.

Baaske, U.P., 2005. Sequence stratigraphy, sedimentology and provenance of the Upper Cretaceous siliciclastic sediments of South Jordan (Dissertation). Universität Stuttgart, Stuttgart.

Barrier, E., Vrielynck, B., Brouillet, J.F., Brunet, M.F., Contributors, Angiolini L., Kaveh, F., Plunder, A., Poisson, A., Pourteau, A., Robertson, A., Shekawat, R., Sosson, M., Zanchi, A., 2018. Paleotectonic Reconstruction of the Central Tethyan Realm. Tectono-Sedimentary-Palinspastic maps from Late Permian to Pliocene. CCGM/CGMW, Paris. http://www.ccgm.org. Atlas of 20 maps (scale: 1/15 000 000).

Bauer, J., Kuss, J., Steuber, T., 2003. Sequence architecture and carbonate platform configuration (Late Cenomanian–Santonian), Sinai, Egypt. Sedimentology 50, 387–414. https://doi.org/10.1046/j.1365-3091.2003.00549.x.

Behar, F., Beaumont, V., De, B., Penteado, H.L., 2001. Rock-Eval 6 Technology: Performances and Developments. Oil & Gas Science and Technology - Rev. IFP 56, 111–134. https://doi.org/10.2516/ogst:2001013.

Bein, A., Weiler, Y., 1976. The Cretaceous Talme Yafe Formation: a contour current shaped sedimentary prism of calcareous detritus at the continental margin of the Arabian Craton. Sedimentology 23, 511–532. https://doi.org/10.1111/j.1365-3091.1976.tb00065.x.

Bender, F., 1974. Explanatory Notes on the Geological Map of the Wadi Araba, Jordan. Schweizerbart Science Publishers, Stuttgart, Germany.

Berndt, R., 2002. Palaeoecology and taxonomy of the macrobenthic fauna from the Upper Cretaceous Ajlun Group, southern Jordan (Dissertation). Universität Würzburg, Würzburg.

Bomou, B., Adatte, T., Arnaud-Vanneau, A., 2020. Guerrero-Morelos carbonate platform response to the Caribbean-Colombian Cretaceous large igneous province during Cenomanian–Turonian oceanic anoxic event 2. In: Mass Extinctions, Volcanism, and Impacts: New Developments. Geological Society of America, pp. 105–136. https://doi.org/10.1130/2019.2544(05.

Brand, W.A., Assonov, S.S., Coplen, T.B., 2010. Correction for the 17O interference in δ(13C) measurements when analyzing CO2 with stable isotope mass spectrometry (IUPAC Technical Report). Pure and Applied Chemistry 82, 1719–1733. https://doi.org/10.1351/PAC-REP-09-01-05.

Bromhead, A.D., van Buchem, F.S.P., Simmons, M.D., Davies, R.B., 2022. Sequence stratigraphy, paleogeography and petroleum plays of the Cenomanian – Turonian succession of the Arabian Plate: An updated synthesis. Journal of Petroleum Geology 45, 119–161. https://doi.org/10.1111/jpg.12810.

Buchbinder, B., Benjamini, C., Lipson-Benitah, S., 2000. Sequence development of Late Cenomanian–Turonian carbonate ramps, platforms and basins in Israel. Cretaceous Research 21, 813–843. https://doi.org/10.1006/cres.2000.0228.

Cramer, B.D., Jarvis, I., 2020. Carbon Isotope Stratigraphy. In: Geologic Time Scale 2020. Elsevier, pp. 309–343. https://doi.org/10.1016/B978-0-12-824360-2.00011-5.

Droste, H., 2010. High-resolution seismic stratigraphy of the Shu'aiba and Natih formations in the Sultanate of Oman: implications for Cretaceous epeiric carbonate platform systems. Geological Society, London, Special Publications 329, pp. 145–162. https://doi.org/10.1144/SP329.7.

Dunham, R.J., 1962. Classification of Carbonate Rocks According to Depositional Texture. In: Ham, W.E. (Ed.), Classification of Carbonate Rocks—A Symposium. American Association of Petroleum Geologists, Tulsa, pp. 108–121.

El-Sabbagh, A., Tantawy, A.A., Keller, G., Khozyem, H., Spangenberg, J., Adatte, T., Gertsch, B., 2011. Stratigraphy of the Cenomanian–Turonian Oceanic Anoxic Event OAE2 in shallow shelf sequences of NE Egypt. Cretaceous Research 32, 705–722. https://doi.org/10.1016/j.cretres.2011.04.006.

Embry, A., Klovan, J., 1971. A late Devonian reef tract on northeastern Banks Island, N.W.T. Bulletin of Canadian Petroleum Geology 19, 730–781.

Farouk, S., Ahmad, F., Powell, J.H., 2017. Cenomanian–Turonian stable isotope signatures and depositional sequences in northeast Egypt and central Jordan. Journal of Asian Earth Sciences 134, 207–230. https://doi.org/10.1016/j.jseaes.2016.11.021.

Farouk, S., Abdeldaim, A., Ahmad, F., Ruebsam, W., Alsuwaidi, M., Al-Kahtany, K., 2025. Cyclostratigraphy of the Cenomanian-Turonian boundary in Jordan. Marine and Petroleum Geology 180, 107463. https://doi.org/10.1016/j.marpetgeo.2025.107463.

Flexer, A., Rosenfeld, A., Lipson-Benitah, S., Honigstein, A., 1986. Relative sea level changes during the Cretaceous in Israel. American Association of Petroleum Geologists Bulletin 70, 1685–1699.

Forster, A., Schouten, S., Moriya, K., Wilson, P.A., Sinninghe Damsté, J.S., 2007. Tropical warming and intermittent cooling during the Cenomanian/Turonian oceanic anoxic event 2: Sea surface temperature records from the equatorial Atlantic. Paleoceanography 22, PA1219. https://doi.org/10.1029/2006PA001349.

Frank, R., Buchbinder, B., Benjamini, C., 2010. The mid-Cretaceous carbonate system of northern Israel: facies evolution, tectono-sedimentary configuration and global control on the central Levant margin of the Arabian Plate. Geological Society, London, Special Publications 341 (7), 133–169. https://doi.org/10.1144/SP341.

Friedrich, O., Norris, R.D., Erbacher, J., 2012. Evolution of middle to Late Cretaceous oceans—A 55 m.y. record of Earth's temperature and carbon cycle. Geology 40 (1), 107–110. https://doi.org/10.1130/G32701.

Frizon De Lamotte, D., Raulin, C., Mouchot, N., Wrobel-Daveau, J.-C., Blanpied, C., Ringenbach, J.-C., 2011. The southernmost margin of the Tethys realm during the Mesozoic and Cenozoic: Initial geometry and timing of the inversion processes. Tectonics 30. https://doi.org/10.1029/2010TC002691.

Grélaud, C., Razin, P., Homewood, P.W., Schwab, A.M., 2006. Development of incisions on a periodically emergent carbonate platform (Natih Formation, Late Cretaceous, Oman). Journal of Sedimentary Research 76, 647–669. https://doi.org/10.2110/jsr.2006.058.

Grélaud, C., Razin, P., Homewood, P., 2010. Channelized systems in an inner carbonate platform setting: differentiation between incisions and tidal channels (Natih Formation, Late Cretaceous, Oman). Geological Society, London, Special Publications 329, 163–186. https://doi.org/10.1144/SP329.8.

Grosheny, D., Ferry, S., Lecuyer, C., Merran, Y., Mroueh, M., Granier, B., 2017. The Cenomanian-Turonian Boundary Event (CTBE) in northern Lebanon as compared to regional data – Another set of evidences supporting a short-lived tectonic pulse coincidental with the event? Palaeogeography, Palaeoclimatology, Palaeoecology 487, 447–461. https://doi.org/10.1016/j.palaeo.2017.09.031.

Hairapetian, V., Wilmsen, M., Ahmadi, A., Shojaei, Z., Berensmeier, M., Majidifard, M.R., 2018. Integrated stratigraphy, facies analysis and correlation of the upper Albian–lower Turonian of the Esfahan area (Iran): Unravelling the conundrum of the so-called "Glauconitic Limestone.". Cretaceous Research 90, 391–411. https://doi.org/10.1016/j.cretres.2018.06.014.

Hajikazemi, E., Al-Aasm, I.S., Coniglio, M., 2012. Chemostratigraphy of Cenomanian–Turonian carbonates of the Sarvak Formation, southern Iran. Journal of Petroleum Geology 35, 187–205. https://doi.org/10.1111/j.1747-5457.2012.00525.x.

Haq, B.U., 2014. Cretaceous eustasy revisited. Global and Planetary Change 113, 44–58. https://doi.org/10.1016/j.gloplacha.2013.12.007.

Hardy, C., Homberg, C., Eyal, Y., Barrier, É., Müller, C., 2010. Tectonic evolution of the southern Levant margin since Mesozoic. Tectonophysics 494, 211–225. https://doi.org/10.1016/j.tecto.2010.09.007.

Hennhoefer, D., Al Suwaidi, A., Bottini, C., Helja, E., Steuber, T., 2019. The Albian to Turonian carbon isotope record from the Shilaif Basin (United Arab Emirates) and its regional and intercontinental correlation. Sedimentology 66, 536–555. https://doi.org/10.1111/sed.12493.

Hennhoefer, D., Al Suwaidi, A., Steuber, T., 2020. The onset of Oceanic Anoxic Event 2 on the Arabian Shelf – mechanisms between organic matter deposition, sea-level, and palaeoceanography (Shilaif Basin, United Arab Emirates). Newsletters on Stratigraphy 53, 121–139. https://doi.org/10.1127/nos/2019/0504.

Huber, B.T., Norris, R.D., MacLeod, K.G., 2002. Deep-sea paleotemperature record of extreme warmth during the Cretaceous. Geology 30, 123–126. https://doi.org/10.1130/0091-7613(2002)030<0123:DSPROE>2.0.CO;2.

Huber, B.T., MacLeod, K.G., Watkins, D.K., Coffin, M.F., 2018. The rise and fall of the Cretaceous Hot Greenhouse climate. Global and Planetary Change 167, 1–23. https://doi.org/10.1016/j.gloplacha.2018.04.004.

Huck, S., Heimhofer, U., Immenhauser, A., Weissert, H., 2013. Carbon-isotope stratigraphy of Early Cretaceous (Urgonian) shoal-water deposits: Diachronous changes in carbonate-platform production in the north-western Tethys. Sedimentary Geology 290, 157–174. https://doi.org/10.1016/j.sedgeo.2013.03.016.

Immenhauser, A., Della Porta, G., Kenter, J.A.M., Bahamonde, J.R., 2003. An alternative model for positive shifts in shallow-marine carbonate $\delta^{13}C$ and $\delta^{18}O$. Sedimentology 50, 953–959. https://doi.org/10.1046/j.1365-3091.2003.00590.x.

Immenhauser, A., Holmden, C., Patterson, W., 2008. Interpreting the carbon-isotope record of ancient shallow epeiric seas: Lessons from the recent. In: Pratt, B.R., Holmden, C. (Eds.), Dynamics of Epeiric Seas, 48. Geological Association of Canada-Special Paper, pp. 137–174.

Jarvis, I., Gale, A.S., Jenkyns, H.C., Pearce, M.A., 2006. Secular variation in Late Cretaceous carbon isotopes: a new $\delta^{13}C$ carbonate reference curve for the Cenomanian–Campanian (99.6–70.6 Ma). Geological Magazine 143, 561–608. https://doi.org/10.1017/S0016756806002421.

Jarvis, I., Trabucho-Alexandre, J., Gröcke, D.R., Uličný, D., Laurin, J., 2015. Intercontinental correlation of organic carbon and carbonate stable isotope records: evidence of climate and sea-level change during the Turonian (Cretaceous). The Depositional Record 1 (6), 53–90. https://doi.org/10.1002/dep2.

Jenkyns, H.C., 2010. Geochemistry of oceanic anoxic events. Geochemistry, Geophysics, Geosystems 11, Q03004. https://doi.org/10.1029/2009GC002788.

Jones, M.M., Sageman, B.B., Selby, D., Jacobson, A.D., Batenburg, S.J., Riquier, L., MacLeod, K.G., Huber, B.T., Bogus, K.A., Tejada, M.L.G., Kuroda, J., Hobbs, R.W., 2023. Abrupt episode of mid-Cretaceous ocean acidification triggered by massive volcanism. Nature Geoscience 16, 169–174. https://doi.org/10.1038/s41561-022-01115-w.

Kalanat, B., Vaziri-Moghaddam, H., 2019. The Cenomanian/Turonian boundary interval deep-sea deposits in the Zagros Basin (SW Iran): Bioevents, carbon isotope record and palaeoceanographic model. Palaeogeography, Palaeoclimatology, Palaeoecology 533, 109238. https://doi.org/10.1016/j.palaeo.2019.109238.

Kalifi, A., Messaoud, J.H., Baby, G., Ibrahim, K., Powell, J.H., van Buchem, F., 2025. Tectono-stratigraphic evolution of the Late Cretaceous-Eocene of Jordan and implications for the Arabian Plate convergent margin phase. Marine and Petroleum Geology 181, 107525. https://doi.org/10.1016/j.marpetgeo.2025.107525.

Křížová, B., Consorti, L., Cardelli, S., Schmitt, K.E., Brombin, V., Franceschi, M., Tunis, G., Bonini, L., Frijia, G., 2024. Late Cretaceous (Cenomanian-Turonian) temperature evolution and biotic response in the Adriatic Carbonate Platform region of Friuli, northeast Italy. Palaeogeography, Palaeoclimatology, Palaeoecology 637, 111995. https://doi.org/10.1016/j.palaeo.2023.111995.

Kuss, J., 1992a. The Aptian-Paleocene shelf carbonates of northeast Egypt and southern Jordan: Establishment and break-up of carbonate platforms along the southern Tethyan Shores. Zeitschrift der Deutschen Geologischen Gesellschaft 143, 107–132. https://doi.org/10.1127/zdgg/143/1992/107.

Kuss, J., 1992b. Facies and stratigraphy of Cretaceous limestones from northeast Egypt, Sinai, and southern Jordan. In: Geology of the Arab World. Cairo University, Cairo, pp. 283–301.

Kuss, J., Bassiouni, A., Bauer, J., Bachmann, M., Marzouk, A., Scheibner, C., Schulze, F., 2003. Cretaceous — Paleogene Sequence Stratigraphy of the Levant Platform (Egypt, Sinai, Jordan). In: Gili, E., Hédi Negra, M., Skelton, P.W. (Eds.), North African Cretaceous Carbonate Platform Systems. Springer, Netherlands, Dordrecht, pp. 171–187. https://doi.org/10.1007/978-94-010-0015-4_10.

Lawa, F.A., Mohammed, I., Farouk, S., Ahmad, F., Faris, M., Tanner, L., Al-Kahtany, K., 2023. Stratigraphic architecture of the Tethyan Cenomanian-Turonian succession and OAE2 in the Dokan Area, Kurdistan Region, northeast Iraq. Journal of African Earth Sciences 207, 105064. https://doi.org/10.1016/j.jafrearsci.2023.105064.

Li, Y.-X., Liu, X., Selby, D., Liu, Z., Montañez, I.P., Li, X., 2022. Enhanced ocean connectivity and volcanism instigated global onset of Cretaceous Oceanic Anoxic Event 2 (OAE2) ~94.5 million years ago. Earth and Planetary Science Letters 578, 117331. https://doi.org/10.1016/j.epsl.2021.117331.

Masri, M., 1963. Report on the geology of the Amman-Zerqa area. Central Water Authority Report, Amman, Jordan. Central Water Authority. Amman, Jordan.

Matsumoto, H., Coccioni, R., Frontalini, F., Shirai, K., Jovane, L., Trindade, R., Savian, J.F., Kuroda, J., 2022. Mid-Cretaceous marine Os isotope evidence for heterogeneous cause of oceanic anoxic events. Nature Communications 13, 239. https://doi.org/10.1038/s41467-021-27817-0.

Meister, C., Piuz, A., 2015. Cretaceous ammonites from the Sultanate of Oman (Adam Foothills). GeoArabia 20, 19–74. https://doi.org/10.2113/geoarabia200219.

Messaoud, J.H., Kalifi, A., Alibrahim, A., Ibrahim, K., Chirakal, T., Ardilla-Sanchez, M., Leila, W.A., Ben Chabaane, N., Grélaud, C., Powell, J.H., van Buchem, F., 2025. Chronostratigraphy of the mixed Upper Cretaceous deposits at the northern margin of the Arabian Plate (Jordan). Newsletters on Stratigraphy 58, 161–201. https://doi.org/10.1127/nos/2025/0858.

Metzner, N., Niebuhr, B., Pürner, T., Wilmsen, M., 2023. Chemostratigraphy of the lower Danubian Cretaceous Group (Cenomanian–lower Turonian, Bavaria, SE Germany)—A new carbon isotope reference curve and inter-basinal correlation. Cretaceous Research 149, 105568. https://doi.org/10.1016/j.cretres.2023.105568.

Miller, K.G., Sugarman, P.J., Browning, J.V., Kominz, M.A., Olsson, R.K., Feigenson, M.D., Hernández, J.C., 2004. Upper Cretaceous sequences and sea-level history, New Jersey Coastal Plain. Geological Society of America Bulletin 116 (1), 368. https://doi.org/10.1130/B25279.

Miller, K.G., Wright, J.D., Browning, J.V., 2005. Visions of ice sheets in a greenhouse world. Marine Geology 217, 215–231. https://doi.org/10.1016/j.margeo.2005.02.007.

Morsi, A.-M.M., Wendler, J.E., 2010. Biostratigraphy, palaeoecology and palaeogeography of the Middle Cenomanian-Early Turonian Levant Platform in Central Jordan based on ostracods. Geological Society, London, Special Publications 341 (9), 187–210. https://doi.org/10.1144/SP341.

Nagm, E., Farouk, S., Ahmad, F., 2017. The Cenomanian–Turonian boundary in Jordan: Ammonite biostratigraphy and faunal turnover. Geobios 50, 37–47. https://doi.org/10.1016/j.geobios.2016.11.002.

Norris, R.D., Bice, K.L., Magno, E.A., Wilson, P.A., 2002. Jiggling the tropical thermostat in the Cretaceous hothouse. Geology 30, 299–302. https://doi.org/10.1130/0091-7613(2002)030<0299:JTTTIT>2.0.CO;2.

O'Brien, C.L., Robinson, S.A., Pancost, R.D., Sinninghe Damsté, J.S., Schouten, S., Lunt, D.J., Alsenz, H., Bornemann, A., Bottini, C., Brassell, S.C., Farnsworth, A., Forster, A., Huber, B.T., Inglis, G.N., Jenkyns, H.C., Linnert, C., Littler, K., Markwick, P., McAnena, A., Mutterlose, J., Naafs, B.D.A., Püttmann, W., Sluijs, A., van Helmond, N.A.G.M., Vellekoop, J., Wagner, T., Wrobel, N.E., 2017. Cretaceous sea-surface temperature evolution: Constraints from TEX86 and planktonic foraminiferal oxygen isotopes. Earth-Science Reviews 172, 224–247. https://doi.org/10.1016/j.earscirev.2017.07.012.

Parente, M., Frijia, G., Di Lucia, M., Jenkyns, H.C., Woodfine, R.G., Baroncini, F., 2008. Stepwise extinction of larger foraminifers at the Cenomanian-Turonian boundary: A shallow-water perspective on nutrient fluctuations during Oceanic Anoxic Event 2 (Bonarelli Event). Geology 36, 715–718. https://doi.org/10.1130/G24893A.1.

Paul, C.R.C., Lamolda, M.A., 2009. Testing the precision of bioevents. Geological Magazine 146, 625–637. https://doi.org/10.1017/S0016756809006463.

Petrizzo, M.R., Parente, M., Falzoni, F., Bottini, C., Frijia, G., Steuber, T., Erba, E., 2025. Calcareous plankton and shallow-water benthic biocalcifiers: Resilience and extinction across the Cenomanian-Turonian Oceanic Anoxic Event 2. Palaeogeography, Palaeoclimatology, Palaeoecology 668, 112891. https://doi.org/10.1016/j.palaeo.2025.112891.

Philip, J.M., Airaud-Crumiere, C., 1991. The demise of the rudist-bearing carbonate platforms at the Cenomanian/Turonian boundary: a global control. Coral Reefs 10, 115–125. https://doi.org/10.1007/BF00571829.

Philip, J., Borgomano, J., Al-Maskiry, S., 1995. Cenomanian-Early Turonian carbonate platform of northern Oman: stratigraphy and palaeo-environments. Palaeogeography, Palaeoclimatology, Palaeoecology 119, 77–92. https://doi.org/10.1016/0031-0182(95)00061-5.

Philip, J., Negra, M.H., Bachari, M., 2024. Upper Cenomanian caprinulid-radiolitid rudists (Bivalvia) from the Gattar Member of Jebel el Kebar (central Tunisia): Stratigraphical implications and palaeobiogeographical relationships with coeval rudist-assemblages from carbonate platforms of the southern Tethyan margin. Cretaceous Research 153, 105713. https://doi.org/10.1016/j.cretres.2023.105713.

Powell, J.H., 1989. Stratigraphy and sedimentation of the Phanerozoic rocks in central and southern Jordan. Bulletin 11, Geology Directorate, Natural Resources Authority (Ministry of Energy and Mineral Resources) Amman, HK of Jordan. Part B: Kurnub, Ajlun and Belqa Groups.

Powell, J.H., Moh'd, B.K., 2011. Evolution of Cretaceous to Eocene alluvial and carbonate platform sequences in central and south Jordan. GeoArabia 16, 29–82. https://doi.org/10.2113/geoarabia160429.
Quennell, A.M., 1951. The Geology and Mineral Resources of (former) Transjordan. Colon. Geol. Min. Resources 2, 85–115.
Quennell, A.M., 1959. Tectonics of the Dead Sea Rift. 20th International Geological Congress, Mexico, Assoc. Serv. Geol. Afr. 385–405.
Ray, D.C., van Buchem, F.S.P., Baines, G., Davies, A., Gréselle, B., Simmons, M.D., Robson, C., 2019. The magnitude and cause of short-term eustatic Cretaceous sea-level change: A synthesis. Earth-Science Reviews 197, 102901. https://doi.org/10.1016/j.earscirev.2019.102901.
Razin, P., Grélaud, C., van Buchem, F., 2017. The mid-Cretaceous Natih Formation in Oman: A model for carbonate platforms and organic-rich intrashelf basins. AAPG Bulletin 101, 515–522. https://doi.org/10.1306/011817DIG17030.
Robinson, S.A., Dickson, A.J., Pain, A., Jenkyns, H.C., O'Brien, C.L., Farnsworth, A., Lunt, D.J., 2019. Southern Hemisphere sea-surface temperatures during the Cenomanian–Turonian: Implications for the termination of Oceanic Anoxic Event 2. Geology 47, 131–134. https://doi.org/10.1130/G45842.1.
Sahagian, D., Pinous, O., Olferiev, A., Zakharov, V., 1996. Eustatic Curve for the Middle Jurassic-Cretaceous Based on Russian Platform and Siberian Stratigraphy: Zonal Resolution. AAPG Bulletin 80, 1433–1458. https://doi.org/10.1306/64ED9A56-1724-11D7-8645000102C1865D.
Sass, E., Bein, A., 1982. The Cretaceous carbonate platform in Israel. Cretaceous Research 3, 135–144. https://doi.org/10.1016/0195-6671(82)90014-3.
Schlanger, S.O., Jenkyns, H., 1976. Cretaceous oceanic anoxic events: causes and consequences. Geologie en Mijnbouw 55 (3–4), 179–184.
Schlanger, S.O., Arthur, M.A., Jenkyns, H.C., Scholle, P.A., 1987. The Cenomanian-Turonian Oceanic Anoxic Event, I. In: Stratigraphy and distribution of organic carbon-rich beds and the marine δ^{13} C excursion. Geological Society, London, Special Publications 26, pp. 371–399. https://doi.org/10.1144/GSL.SP.1987.026.01.24.
Scholle, P.A., Arthur, M.A., 1980. Carbon Isotope Fluctuations in Cretaceous Pelagic Limestones: Potential Stratigraphic and Petroleum Exploration Tool. AAPG Bulletin 64. https://doi.org/10.1306/2F91892D-16CE-11D7-8645000102C1865D.
Schulze, F., Lewy, Z., Kuss, J., Gharaibeh, A., 2003. Cenomanian-Turonian carbonate platform deposits in west central Jordan. International Journal of Earth Sciences 92, 641–660. https://doi.org/10.1007/s00531-003-0339-6.
Schulze, F., Marzouk, A.M., Bassiouni, M.A.A., Kuss, J., 2004. The late Albian–Turonian carbonate platform succession of west-central Jordan: stratigraphy and crises. Cretaceous Research 25, 709–737. https://doi.org/10.1016/j.cretres.2004.06.008.
Schulze, F., Kuss, J., Marzouk, A., 2005. Platform configuration, microfacies and cyclicities of the upper Albian to Turonian of west-central Jordan. Facies 50, 505–527. https://doi.org/10.1007/s10347-004-0032-7.
Scotese, C.R., 2014. Atlas of Late Cretaceous Maps, PALEOMAP Atlas for ArcGIS, volume 2, The Cretaceous, Maps 16 – 22, Mollweide Projection. PALEOMAP Project, Evanston, IL. https://doi.org/10.13140/2.1.4691.3284.
Searle, M., Rioux, M., Garber, J.M., 2022. One line on the map: A review of the geological history of the Semail Thrust, Oman-UAE mountains. Journal of Structural Geology 158, 104594. https://doi.org/10.1016/j.jsg.2022.104594.
Segev, A., Lyakhovsky, V., Weinberger, R., 2014. Continental transform–rift interaction adjacent to a continental margin: The Levant case study. Earth-Science Reviews 139, 83–103. https://doi.org/10.1016/j.earscirev.2014.08.015.
Sharland, P.R., Archer, R., Casey, D.M., Davies, R.B., Hall, S.H., Heward, A.P., Horbury, A.D., Simmons, M.D., 2001. Arabian Plate Sequence Stratigraphy. GeoArabia Special Publication 2, 371.
Simmons, M.D., Bidgood, M.D., Davies, R.B., Droste, H., Levell, B., Razin, P., van Buchem, F.S.P., 2025. Intra-Turonian stratigraphic reorganization on the Arabian Plate. Geological Society, London, Special Publications 545, 431–491. https://doi.org/10.1144/SP545-2023-207.
Sooraj, C.P., Gupta, S., Punekar, J., 2024. Spatio-temporal variability in microfossil and geochemical records of Cenomanian-Turonian oceanic anoxic event-2: a review. Journal of Palaeogeography 13, 646–674. https://doi.org/10.1016/j.jop.2024.06.002.
Steuber, T., Löser, H., Mutterlose, J., Parente, M., 2023. Biogeodynamics of Cretaceous marine carbonate production. Earth-Science Reviews 238, 104341. https://doi.org/10.1016/j.earscirev.2023.104341.
Swart, P.K., 2015. The geochemistry of carbonate diagenesis: The past, present and future. Sedimentology 62, 1233–1304. https://doi.org/10.1111/sed.12205.
Swart, P.K., Burns, S.J., Leder, J.J., 1991. Fractionation of the stable isotopes of oxygen and carbon in carbon dioxide during the reaction of calcite with phosphoric acid as a function of temperature and technique. Chemical Geology: Isotope Geoscience Section 86, 89–96. https://doi.org/10.1016/0168-9622(91)90055-2.
Takashima, R., Selby, D., Yamanaka, T., Kuwahara, Y., Nakamura, H., Sawada, K., Ikeda, M.A., Ando, T., Hayashi, K., Nishida, M., Usami, T., Kameyama, D., Nishi, H., Kuroyanagi, A., Gyawali, B.R., 2024. Large igneous province activity drives oceanic anoxic event 2 environmental change across eastern Asia. Communications Earth & Environment 5, 85. https://doi.org/10.1038/s43247-024-01214-z.
Trabucho Alexandre, J., Tuenter, E., Henstra, G.A., Van Der Zwan, K.J., Van De Wal, R.S.W., Dijkstra, H.A., De Boer, P.L., 2010. The mid-Cretaceous North Atlantic nutrient trap: Black shales and OAEs. Paleoceanography 25, PA4201. https://doi.org/10.1029/2010PA001925.
Turgeon, S.C., Creaser, R.A., 2008. Cretaceous Oceanic Anoxic Event 2 triggered by a massive magmatic episode. Nature 454, 323–326. https://doi.org/10.1038/nature07076.
Vahrenkamp, V.C., 2010. Chemostratigraphy of the Lower Cretaceous Shu'aiba Formation: A δ13C reference profile for the Aptian Stage from the southern Neo-Tethys Ocean. Barremian – Aptian Stratigraphy and Hydrocarbon Habitat of the Eastern Arabian Plate. Special Publication 4 (1), 107–137. Gulf PetroLink, pp.
Vahrenkamp, V.C., 2013. Carbon-isotope signatures of Albian to Cenomanian (Cretaceous) shelf carbonates of the Natih Formation, Sultanate of Oman. GeoArabia 18, 65–82. https://doi.org/10.2113/geoarabia180365.
Valle, B., Dal' Bó, P.F., Mendes, M., Favoreto, J., Rigueti, A.L., Borghi, L., De Oliveira Mendonça, J., Silva, R., 2019. The expression of the Oceanic Anoxic Event 2 (OAE2) in the northeast of Brazil (Sergipe-Alagoas Basin). Palaeogeography, Palaeoclimatology, Palaeoecology 529, 12–23. https://doi.org/10.1016/j.palaeo.2019.05.029.
van Buchem, F.S.P., Razin, P., Homewood, P.W., Philip, J.M., Eberli, G.P., Platel, J.-P., Roger, J., Eschard, R., Desaubliaux, G.M.J., Boisseau, T., Leduc, J.-P., Labourdette, R., Cantaloube, S., 1996. High resolution sequence stratigraphy of the Natih Formation (Cenomanian/Turonian) in northern Oman: Distribution of source rocks and reservoir facies. GeoArabia 1, 65–91. https://doi.org/10.2113/geoarabia010165.
van Buchem, F.S.P., Razin, P., Homewood, P.W., Oterdoom, W.H., Philip, J., 2002. Stratigraphic organization of carbonate ramps and organic-rich intrashelf basins: Natih Formation (middle Cretaceous) of northern Oman. AAPG Bulletin 86, 21–53. https://doi.org/10.1306/61EEDA30-173E-11D7-8645000102C1865D.
van Buchem, F.S.P., Huc, A., Pradier, B., Stephani, M., 2005. Stratigraphic patterns in carbonate source rock distribution: 2th to 4th order control and sediment flux. In: Harris, N.H. (Ed.), The deposition of organic-carbon-rich sediments: models, mechanisms and consequences. SEPM Special Publications 82, pp. 191–223. https://doi.org/10.2110/pec.05.82.0191.
van Buchem, F.S.P., Simmons, M.D., Droste, H.J., Davies, R.B., 2011. Late Aptian to Turonian stratigraphy of the eastern Arabian Plate – depositional sequences and lithostratigraphic nomenclature. Petroleum Geoscience 17, 211–222. https://doi.org/10.1144/1354-079310-061.
Vicedo, V., Piuz, A., 2017. Evolutionary trends and biostratigraphical application of new Cenomanian alveolinoids (Foraminifera) from the Natih Formation of Oman. Journal of Systematic Palaeontology 15, 821–850. https://doi.org/10.1080/14772019.2016.1244709.
Viltres, R., Jónsson, S., Alothman, A.O., Liu, S., Leroy, S., Masson, F., Doubre, C., Reilinger, R., 2022. Present-day motion of the Arabian Plate. Tectonics 41, e2021TC007013. https://doi.org/10.1029/2021TC007013.
Vincent, B., Van Buchem, F.S.P., Bulot, L.G., Jalali, M., Swennen, R., Hosseini, A.S., Baghbani, D., 2015. Depositional sequences, diagenesis and structural control of the Albian to Turonian carbonate platform systems in coastal Fars (SW Iran). Marine and Petroleum Geology 63, 46–67. https://doi.org/10.1016/j.marpetgeo.2015.02.018.
Voigt, S., Erbacher, J., Mutterlose, J., Weiss, W., Westerhold, T., Wiese, F., Wilmsen, M., Wonik, T., 2008. The Cenomanian Turonian of the Wunstorf section (North Germany): global stratigraphic reference section and new orbital time scale for Oceanic Anoxic Event 2. Newsletters on Stratigraphy 43, 65–89. https://doi.org/10.1127/0078-0421/2008/0043-0065.
Walker-Trivett, C.A., Kender, S., Bogus, K.A., Littler, K., Edvardsen, T., Leng, M.J., Lacey, J., Riding, J.B., Millar, I.L., Wagner, D., 2024. Oceanic Anoxic Event 2 triggered by Kerguelen volcanism. Nature Communications 15, 5124. https://doi.org/10.1038/s41467-024-49032-3.
Wang, J., Redfern, J., Bulot, L.G., Taylor, K.G., 2023. Controls on preservation of organic matter during the Cenomanian Ocean Anoxic Event II (OAE2) and Turonian global sea-level rise: Agadir Basin, Morocco. Journal of African Earth Sciences 207, 105069. https://doi.org/10.1016/j.jafrearsci.2023.105069.
Wendler, I., 2013. A critical evaluation of carbon isotope stratigraphy and biostratigraphic implications for Late Cretaceous global correlation. Earth-Science Reviews 126, 116–146. https://doi.org/10.1016/j.earscirev.2013.08.003.
Wendler, J.E., Wendler, I., 2016. What drove sea-level fluctuations during the mid-Cretaceous greenhouse climate? Palaeogeography, Palaeoclimatology, Palaeoecology 441, 412–419. https://doi.org/10.1016/j.palaeo.2015.08.029.
Wendler, J.E., Lehmann, J., Kuss, J., 2010. Orbital time scale, intra-platform basin correlation, carbon isotope stratigraphy and sea-level history of the Cenomanian–Turonian Eastern Levant platform. Geological Society, London, Special Publications 341, Jordan, pp. 171–186. https://doi.org/10.1144/SP341.8.
Wendler, J.E., Meyers, S.R., Wendler, I., Kuss, J., 2014. A million-year-scale astronomical control on Late Cretaceous sea-level. Newsletters on Stratigraphy 47, 1–19. https://doi.org/10.1127/0078-0421/2014/0038.
Wetzel, R., Morton, D.M., 1959. Contribution a la Geologie de la Transjordanie. (No. VII). In: Notes et Memoirs sur le Moyen Orient.
Whittaker, J.E., Jones, R.W., Banner, F.T., 1998. Key Mesozoic Benthic Foraminifera of the Middle East. The Natural History Museum, London.
Wiese, F., Schulze, F., 2005. The upper Cenomanian (Cretaceous) ammonite *Neolobites vibrayeanus* (d'Orbigny, 1841) in the Middle East: taxonomic and palaeoecologic remarks. Cretaceous Research 26, 930–946. https://doi.org/10.1016/j.cretres.2005.06.005.
Wohlwend, S., Hart, M., Weissert, H., 2016. Chemostratigraphy of the Upper Albian to mid-Turonian Natih Formation (Oman) – how authigenic carbonate changes a global pattern. The Depositional Record 2, 97–117. https://doi.org/10.1002/dep2.15.
Wolfart, R., 1959. Geology and hydrogeology of the Irbid district (Hashemite Kingdom of Jordan). Bundesanstalt für Bodenforschung, Hannover.

Appendix A

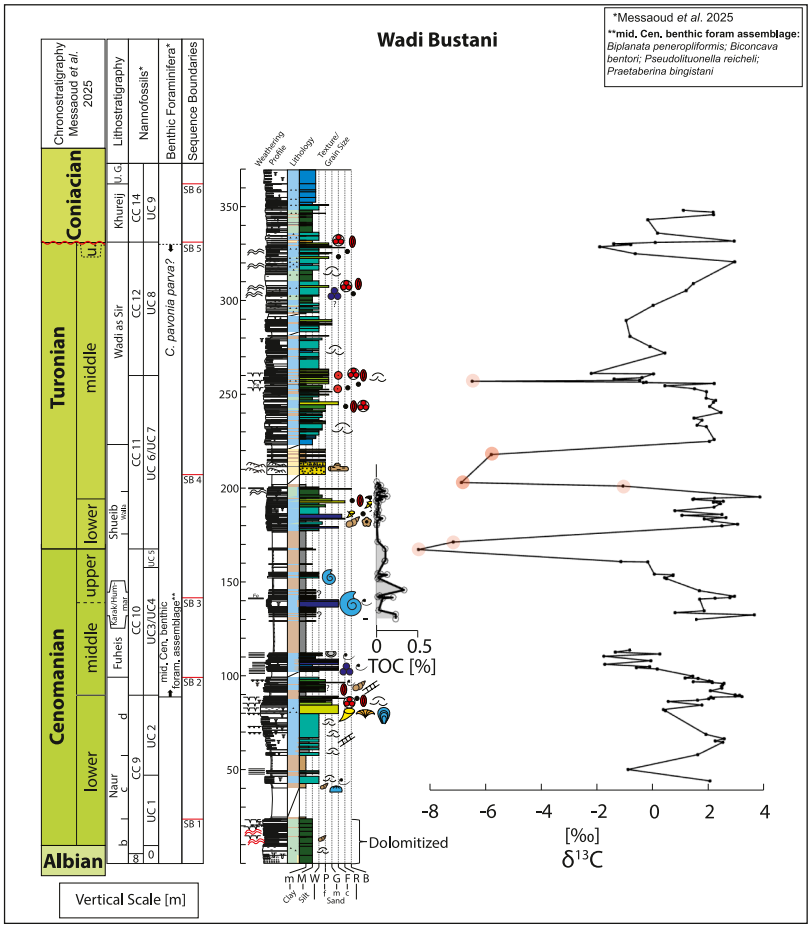
Wadi Bustani
*Messaoud et al. 2025
**mid. Cen. benthic foram assemblage: Biplanata peneropliformis; Biconcava bentori; Pseudolituonella reicheli; Praetaberina bingistani
Chronostratigraphy Messaoud et al. 2025
Lithostratigraphy
Nannofossils*
Benthic Foraminifera*
Sequence Boundaries
Coniacian
Turonian
Cenomanian
Albian
upper
middle
lower
Khureij
Wadi as Sir
Shueib
Fuheis
Naur
C. pavonia parva?
mid. Cen. benthic foram. assemblage**
SB 6
SB 5
SB 4
SB 3
SB 2
SB 1
Weathering Profile
Lithology
Texture/ Grain Size
Dolomitized
0 0.5
TOC [%]
-8 -6 -4 -2 0 2 4
[‰]
δ13C
Vertical Scale [m]
Lower Turonian ammonite fauna: Wadi Karak: Choffaticeras sp. (this study); Wadi Mujib: Choffaticeras segne, see Nagm et al. 2017. Note that lower range of Choffaticeras segne recorded by Nagm et al. 2017 extends into the marls underlying the Walla Member in Wadi Mujib.
Middle? to upper Cenomanian ammonite fauna: Neolobites vibrayeanus from Wadi Karak (this study) and Wadi Mujib (Nagm et al. 2017)
Unassigned ammonites
Lithology
Chert
Chalk
Limestone
Dolomitic limestone
Marls/shales
Organic matter rich
Fines (clay/silt)
Sandstone
Gypsum
Not exposed
Sedimentary Structures
Planar lamination
Wavy lamination
Bioturbation
Nodular texture
Unidirectional crossbedding
Bidirectional crossbedding
Chert nodules
Chicken Wires
Stromatolites
Desiccation cracks
Components
Rudists
Corals
Oysters
Shells
Benthics
Miliolids
Planktics
Echinoids
Sponges
Ammonites
Ooids
Peloids
Oncoids
Algae
Fe-Nodules
Coal Fragments
Gastropods
Surfaces
Erosive contact
Sharp contact
Exposure surface
Bioturbated surface
Firmground
Fe Iron-rich
Other
Fractured
Onlap
First appearance datum
Last appearance datum
Secondary Gypsum
Facies
Red shales
Fluvial SST
Marine SST
Mixed (Siliciclastics - carbonates)
Evaporites
Grainstones (P-G, G)
Packstones
Wackestones (W, W-P)
Mudstones (M, M-W)
Float-/ Rudstones (Muddy, marly)
Float-/ Rudstones (Grainy)
Boundstone
Generic marls
Green marls
OM-Rich
Dolomite
Chalk

Appendix B

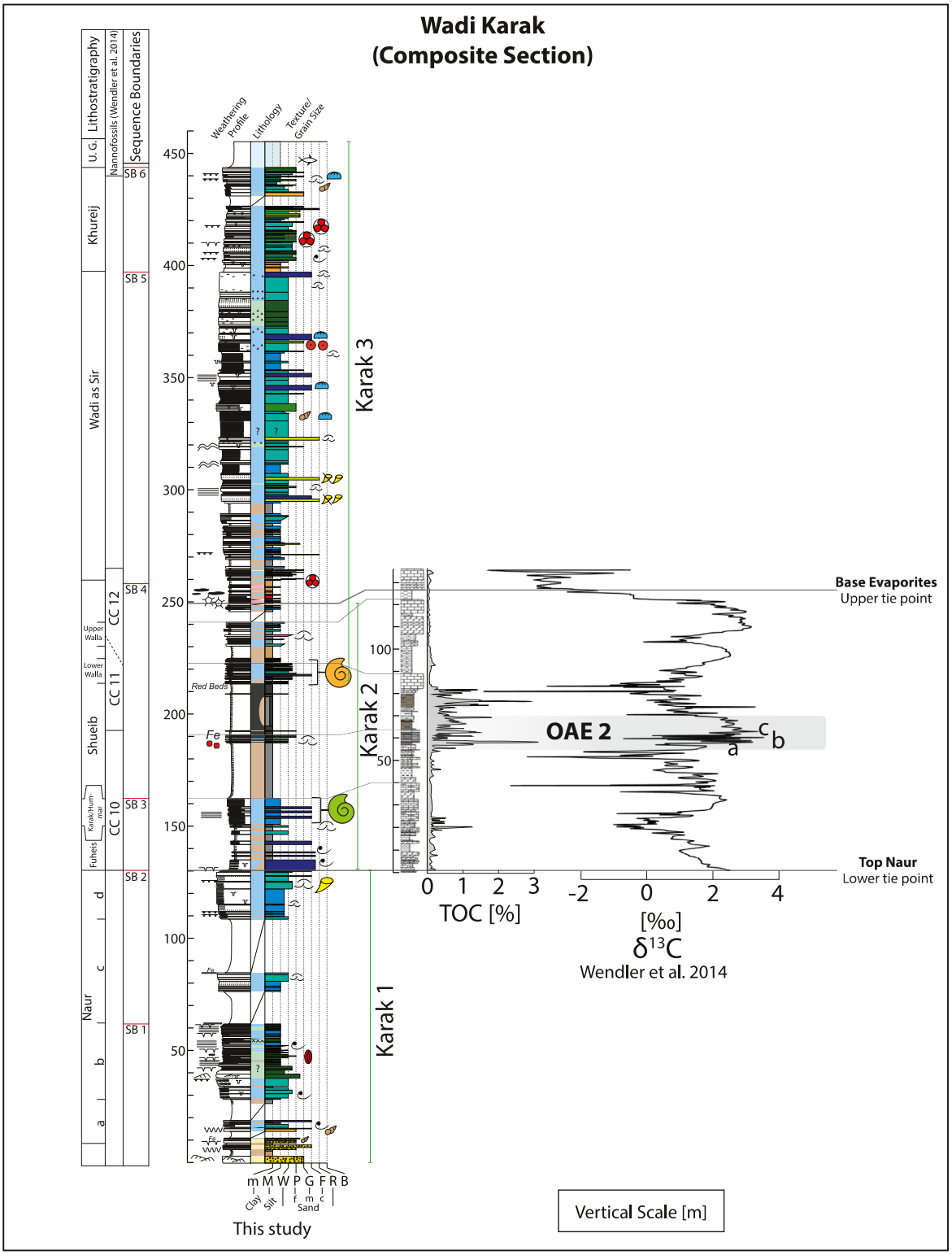
Wadi Karak
(Composite Section)
Lithostratigraphy
U. G.
Nannofossils (Wendler et al. 2014)
Sequence Boundaries
Khureij
Wadi as Sir
Shueib
Fuheis
Naur
SB 6
SB 5
SB 4
SB 3
SB 2
SB 1
CC 12
CC 11
CC 10
Upper Walla
Lower Walla
Karak/Humar
Weathering Profile
Lithology
Texture/ Grain Size
Red Beds
Fe
Karak 3
Karak 2
Karak 1
450
400
350
300
250
200
150
100
50
m M W P G F R B
Clay Silt f m c Sand
This study
Base Evaporites
Upper tie point
OAE 2
a
b
c
Top Naur
Lower tie point
TOC [%]
δ13C [‰]
Wendler et al. 2014
Vertical Scale [m]

Appendix C

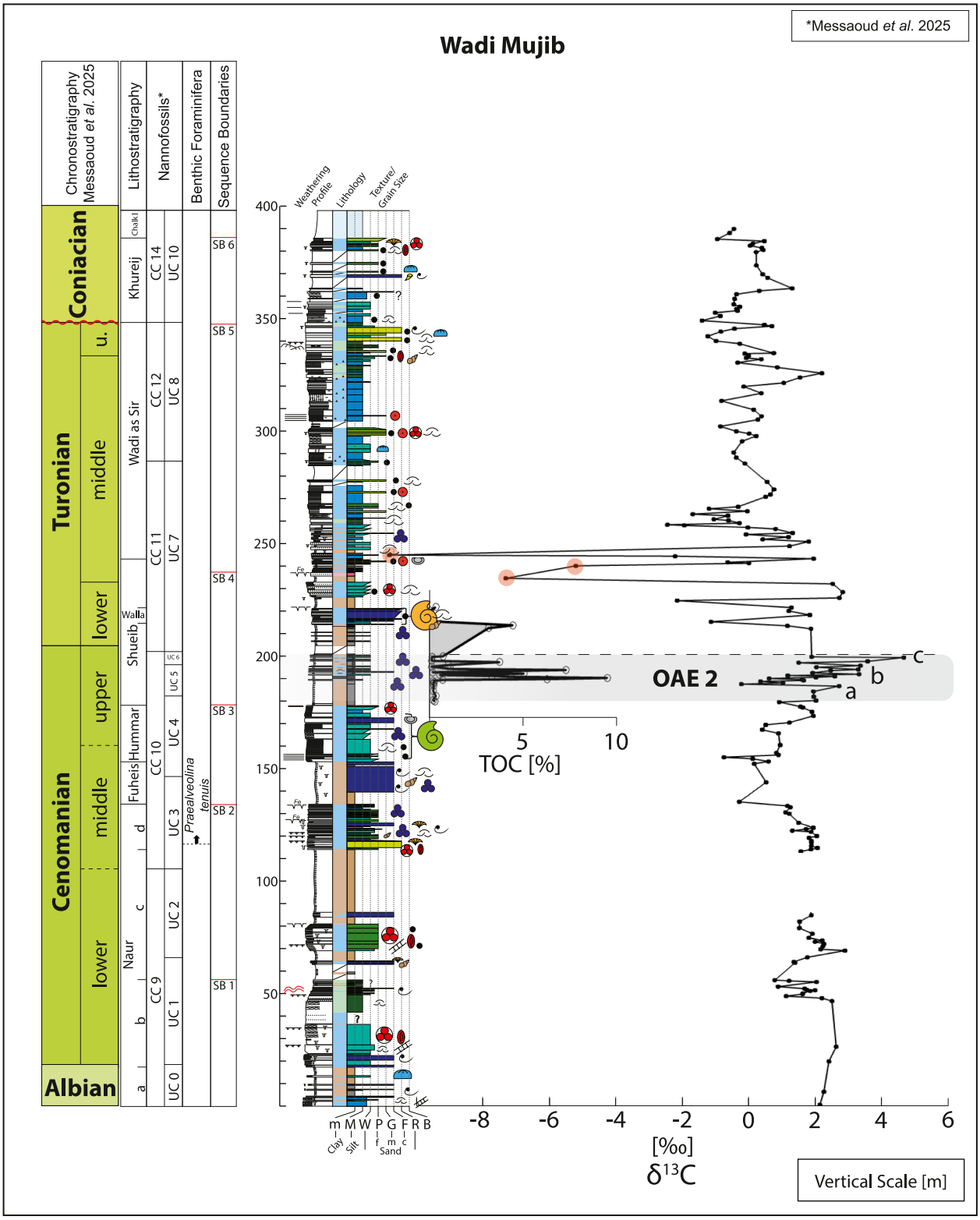
*Messaoud et al. 2025
Wadi Mujib
Chronostratigraphy Messaoud et al. 2025
Lithostratigraphy
Nannofossils*
Benthic Foraminifera
Sequence Boundaries
Coniacian
Turonian
Cenomanian
Albian
upper
middle
lower
Khureij
Wadi as Sir
Shueib
Wasia
Hummar
Fuheis
Naur
Praealveolina tenuis
SB 6
SB 5
SB 4
SB 3
SB 2
SB 1
CC 14
CC 12
CC 11
CC 10
CC 9
UC 10
UC 8
UC 7
UC 6
UC 5
UC 4
UC 3
UC 2
UC 1
UC 0
Weathering Profile
Lithology
Texture/ Grain Size
OAE 2
TOC [%]
δ13C [‰]
Clay
Silt
Sand
Vertical Scale [m]

Appendix D

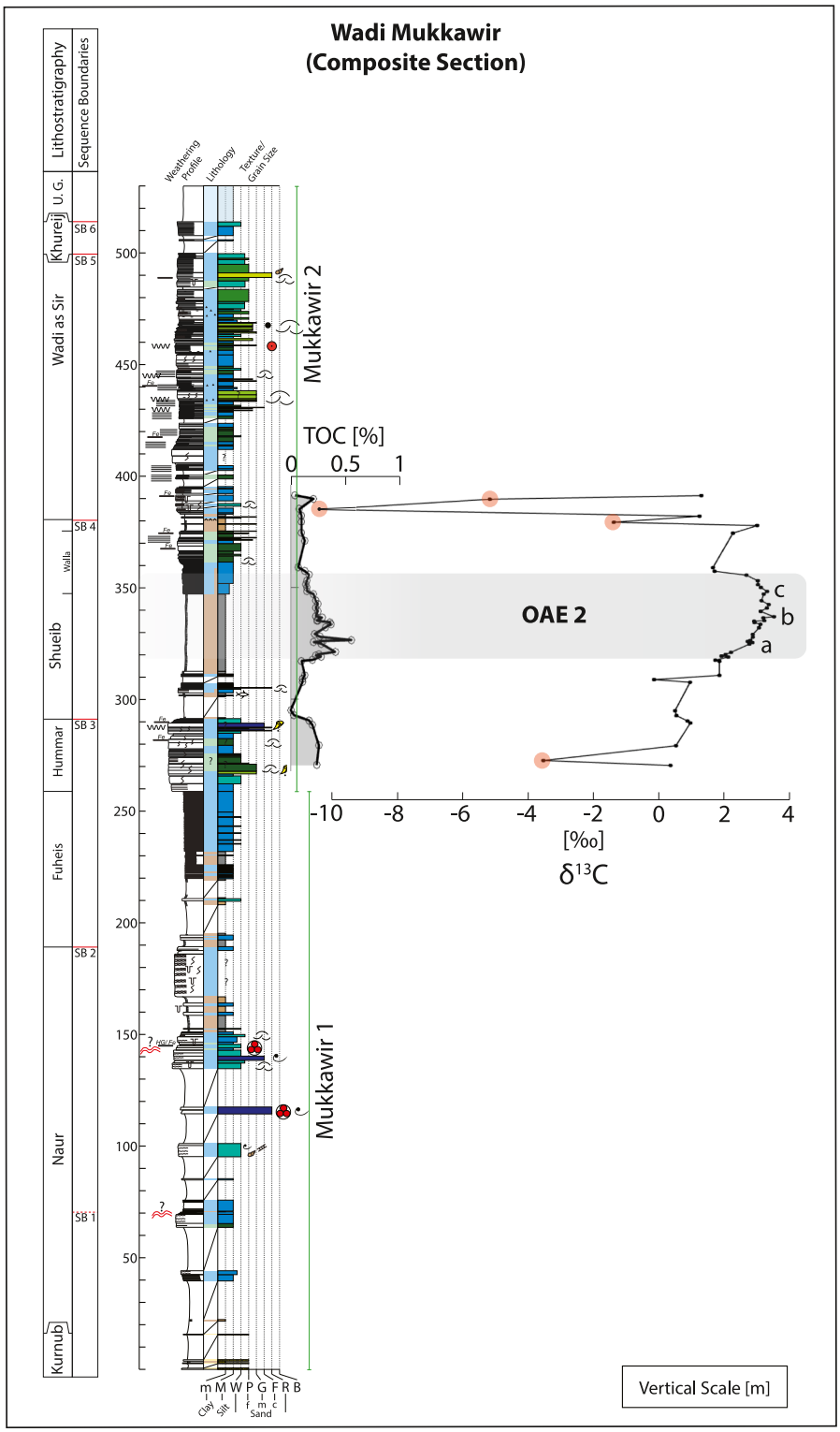
Wadi Mukkawir
(Composite Section)
Lithostratigraphy
Sequence Boundaries
U. G.
Khureij
Wadi as Sir
Shueib
Walla
Hummar
Fuheis
Naur
Kurnub
SB 6
SB 5
SB 4
SB 3
SB 2
SB 1
Weathering Profile
Lithology
Texture/ Grain Size
Mukkawir 2
Mukkawir 1
TOC [%]
0
0.5
1
OAE 2
a
b
c
-10
-8
-6
-4
-2
0
2
4
[‰]
δ13C
500
450
400
350
300
250
200
150
100
50
m M W P G F R B
Clay
Silt
Sand
f m c
Vertical Scale [m]

Appendix E

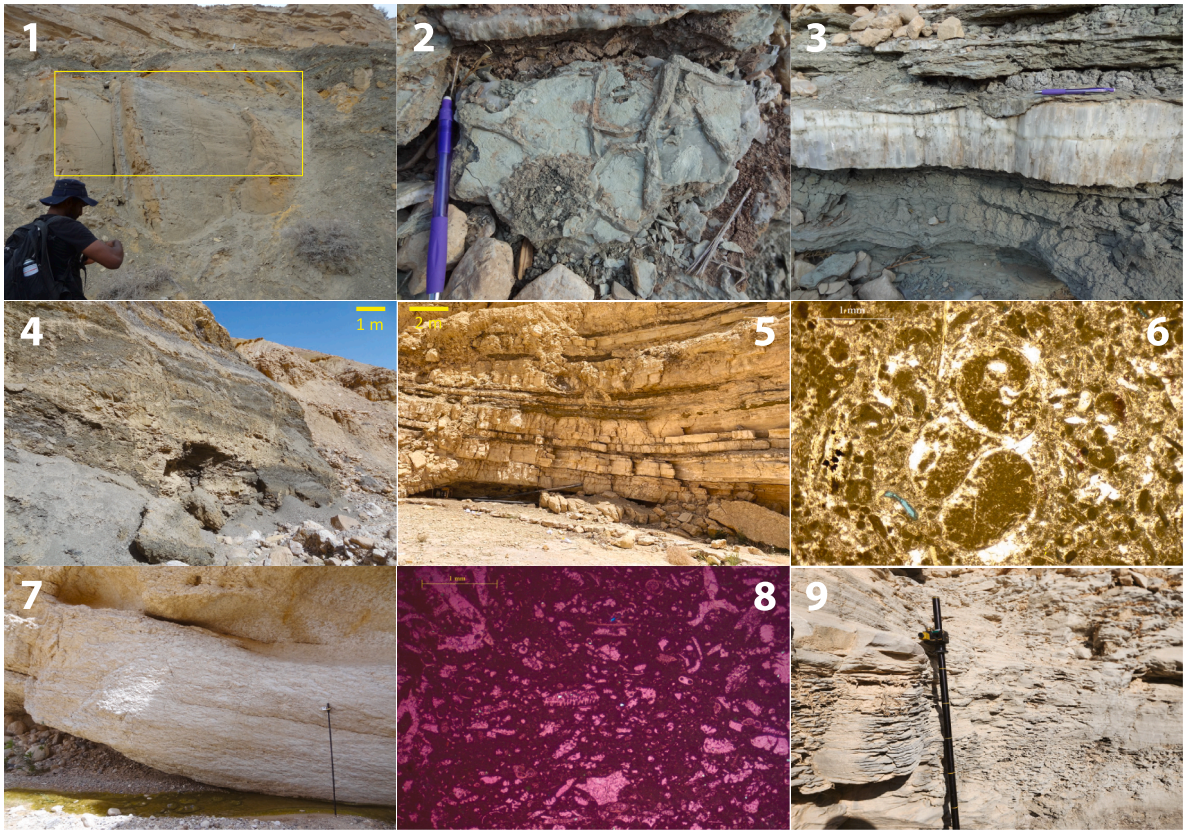

Appendix F. Taxonomic List

Taxon	Author
Acanthoceras jukesbrownei	Spath (1926a)
Acanthoceras rhotomagense	Brongniart (1822)
Acompsoceras	Hyatt (1903)
Biconcava bentori	Hamaoui (1965)
Biplanata peneropliformis	Hamaoui and Saint-Marc (1970)
Calycoceras guerangeri	Spath (1926b)
Choffaticeras	Hyatt (1903)
Choffaticeras segne	Solger (1903)
Collignoniceras woollgari	Mantell (1822)
Corollithion kennedyi	Crux (1981)
Cuneolina pavonia parva?	Henson (1947)
Cunningtoniceras inerme	Pervinquière (1907)
Eiffellithus eximius	Stover (1966); Perch-Nielsen (1968)
Gartnerago nanum	Thierstein (1974)
Gartnerago segmentatum	Stover (1966); Thierstein (1974)
Gartnerago theta	(Black in Black and Barnes (1959); Jakubowski (1986)
Helenea chiastia	Worsley (1971)
Lithraphidites acutus	Verbeek and Manivit in Manivit et al. (1977)
Lucianorhabdus maleformis	Reinhardt (1966)
Mammites nodosoides	Schlüter (1871)
Mantelliceras dixoni	Spath (1926b)
Mantelliceras mantelli	Sowerby, 1814
Marthasterites furcatus	(Deflandre in Deflandre and Fert (1954); Deflandre (1959)
Metoicoceras geslinianum	d'Orbigny (1850)
Micraster coranguinum	Leske (1778)
Micraster cortestudinarium	Goldfuss, 1829
Microrhabdulus decoratus	Deflandre (1959)
Micula staurophora	(Gardet, 1955; Stradner, 1963
Neolobites fourtaui	Pervinquière (1907)
Neolobites vibrayeanus	d'Orbigny (1841)
Praealveolina tenuis	Reichel (1933)
Praetaberina bingistani	Henson (1948)
Pseudolituonella reicheli	Marie (1954)
Quadrum gartneri	Prins and Perch-Nielsen in Manivit et al., 1977
Stoliczkaia dispar	d'Orbigny (1841)
Subprionocyclus neptuni	Geinitz (1849)
Turrilites costatus	Lamarck (1801)
Vascoceras	Choffat (1898)
Watinoceras devonense	Wright and Kennedy (1981)

Black, M. and Barnes, B., 1959. The structure of Coccoliths from the English Chalk. Geological Magazine 96(5), 321-328.

Brongniart, A., 1822. Sur quelques terrains de Craie hors du Bassin de Paris. In: Cuvier, G. and Brongniart A. (Eds.), Description géologique des environs de Paris. Paris: Dufour et d'Ocagne, 80-106.

Choffat, P. 1898., Recueil d'études paléontologiques sur la faune crétacique du Portugal. Les Ammonées du Bellasien des couches à Neolobites vibrayeanus, du Turonien et du Sénonien. Mémoire du Service géologique du Portugal 2, 1-46.

Crux, J. A., 1981. New calcareous nannofossil taxa from the Cretaceous of South East England. Neues Jahrbuch für Geologie und Paläontologie, Monatshefte 1981, 633-640.

d'Orbigny, A., 1841. Paléontologie française: Terrains crétacés. I. Céphalopodes. Masson, Paris, 121-430.

d'Orbigny, A., 1850. Prodrome de Paléontologie stratigraphique universelle des animaux Mollusques et rayonnés faisant suite au cours élémentaire de Paléontologie et de Géologie stratigraphiques 2, 427 pp.

Deflandre, G. and Fert, C., 1954. Observations sur les coccolithophoridés actuels et fossiles en microscopie ordinaire et électronique. Annales de Paléontologie 40, 115-176.

Deflandre, G., 1959. Sur les nannofossiles calcaires et leur systématique. Revue de Micropaléontologie 2, 127-152.

Gardet, M., 1955. Contribution à l'étude des coccolithes des terrains néogènes de l'Algérie. Publications du Service de la Carte Géologique de l'Algérie 5, 477-550.

Geinitz, H.B., 1849. Das Quadersandsteingebirge oder Kreidegebirge in Deutschland. 293 pp. Craz and Gerlach, Freiberg.

Goldfuss, A., 1826-33. Petrefacta Germaniae. Abbildungen und Beschreibungen der Petrefacten Deutschlands und der angrenzenden Laender, 1–252. Duesseldorf: Arnz and Co.

Hamaoui, M., 1965. Biostratigraphy of the Cenomanian type Hazera Formation. Israel Geological Survey, Stratigraphic Sections 2b, 1-27.

Hamaoui, M., Saint-Marc, P., 1970. Microfaunes et microfacies du Cenomanian du Proche-Orient. Bulletin du Centre de Recherches et d'Exploration-Production 4, 257-352.

Henson, F.R.S., 1947. LV.—New Trochamminidæ and Verneuilinidæ from the Middle East. Annals and Magazine of Natural History 14, 605–630.

Henson, F.R.S., 1948. Larger imperforate foraminifera of south-western Asia. Families Lituolidae, Orbitolinidae and Meandropsinidae. British Museum (Natural History), 127 pp.

Hyatt, A., 1903. Pseudoceratites of the Cretaceous. United States Geological Survey Monograph 44, 1-351.

Jakubowski, M., 1986. New calcareous nannofossil taxa from the Lower Cretaceous of the North Sea. INA Newsletter 8(1), 38-42.

Lamarck, J.P.B.A. de M. de, 1801. Système des Animaux sans Vertèbres. Paris, viii + 432 p.

Leske, N.G., 1778. Jacobi Theodori Klein Naturalis dispositio Echinodermatum, edita et descriptionibus novisque inventis et synonymis auctorum aucta, xxii + 278 pp. Lipsiae (Leipzig): G.E. Beer.

Manivit, H., Perch-Nielsen, K., Prins, B. and Verbeek, J. W., 1977. Mid Cretaceous calcareous nannofossil biostratigraphy. Proceedings of the Koninklijke Nederlandse Akademie van Wetenschappen (B) 80(3), 169-181.

Mantell, G.A., 1822. The fossils of the South Downs, or Illustrations of the Geology of Sussex. London: Lupton Relfe, 327 pp.

Marie, P., 1954, Quelques genres nouveaux de foraminifères du Crétacé à facies récifal. Compte Rendu 19th Congrès Géologique International, Alger 1952, sect. 13, fasc. 15, 117-124.

Perch-Nielsen, K., 1968. Der Feinbau und die Klassifikation der Coccolithen aus dem Maastrichtien von Danemark. Biologiske Skrifter, Kongelige Danske Videnskabernes Selskab 16, 1-96.

Pervinquière, L., 1907. Études de paléontologie tunisienne, 1. Céphalopodes des terrains secondaires. Carte géologique de la Tunisie, 1-438.

Reichel, M., 1933. Sur une Alvéoline Cénomanienne du Bassin du Beausset. Eclogae Geologicae Helvetiae 26, 269-280.
Reinhardt, P., 1966. Zur Taxonomie und Biostratigraphie des fossilen Nannoplanktons aus dem Malm, der Kreide und dem Alttertiär Mitteleuropas. Freiberger Forschungshefte C 196, 5-109.
Schlüter, C., 1871. Cephalopoden der oberen deutschen Kreide. Palaeontographica 21, 1-24.
Solger, F., 1903. Über die Jugendentwicklung von Sphenodiscus lenticularis Owen und seine Beziehungen zur Gruppe der Tissotien. Zeitschrift der Deutschen Geologischen Gesellschaft 55, 69-84.
Sowerby J., 1814. The Mineral Conchology of Great Britain. 1, pls. 1-9. London.
Spath, L. F., 1926a. On new ammonites from the English Chalk. Geological Magazine 63, 77-83.
Spath, L. F., 1926b. On the zones of the Cenomanian and the uppermost Albian. Proceedings of the Geologists' Association 37, 420-432.
Stover, L. E., 1966. Cretaceous coccoliths and associated nannofossils from France and the Netherlands. Micropaleontology 12(2), 133-167.
Stover, L. E., 1966. Cretaceous coccoliths and associated nannofossils from France and the Netherlands. Micropaleontology 12(2), 133-167.
Stradner, H., 1963. New contributions to Mesozoic stratigraphy by means of nannofossils. In: Proceedings of the Sixth World Petroleum Congress. Section 1, Paper 4, 167-183.
Thierstein, H. R., 1974. Calcareous nannoplankton - Leg 26, Deep Sea Drilling Project. Initial Reports of the Deep Sea Drilling Project 26, 619-667.
Worsley, T. R., 1971. Calcareous nannofossil zonation of Upper Jurassic and Lower Cretaceous sediments from the Western Atlantic. In: Farinacci, A. (Ed.), Proceedings of the Second Planktonic Conference Roma 1970. Edizioni Tecnoscienza, Rome, 1301-1321.
Wright, C. W. and Kennedy, W. J., 1981. The Ammonoidea of the Plenus Marls and the Middle Chalk. Palaeontographical Society Monographs, 148 pp.